MODELING OF SUSPENSION PLASMA SPRAYING

FARZAD JABBARI

A Thesis

in

the Department

of

Mechanical and Industrial Engineering

Presented in Partial Fulfillment of the Requirements
for the Degree of Master of Applied Science (Mechanical Engineering) at
Concordia University
Montreal, Quebec, Canada

December 2013

CONCORDIA UNIVERSITY

SCHOOL *of*
GRADUATE STUDIES

This is to certify that the thesis prepared

By: Farzad Jabbari

Entitled: **MODELING OF SUSPENSION PLASMA SPRAYING**

and submitted in partial fulfillment of the requirements for the degree of

Master of Applied Science (Mechanical Engineering)

Complies with the regulations of the University and meets the accepted standards with respect to originality and quality.

Signed by the final examining committee:

Dr. Sivakumar Narayanswamy	Chair
Dr. Christian Moreau	Examiner
Dr. Fariborz Haghighat Building, Civil and Environmental Engineering	Examiner External
Dr. A. Dolatabadi and Dr. Rolf Wüthrich	Supervisors

Approved by

Dr. Martin D. Pugh, MASc Program Director
Department of Mechanical and Industrial Engineering

mm/dd/yyyy

Abstract

MODELING OF SUSPENSION PLASMA SPRAYING

Farzad Jabbari

Plasma Spraying is a coating process designed to deposit accelerated molten or semi-molten coating materials on prepared substrates. Suspension Plasma Spraying (SPS) is one type of Plasma Spraying with enhanced characteristics. Numerical modeling of this process helps us to find optimum operating parameters such as suspension injection position and standoff distance for substrates. A three-dimensional model of a plasma spraying system with radial suspension injection is studied in this work. To model turbulent flow of plasma, Reynolds Stress Model (RSM) is utilized. In addition, Lagrangian approach is used to track particles and two-way coupling is used to consider the effect of suspension on the gas flow. It should be mentioned that when mass flow rate of suspension is very high, the plasma plume cannot melt all particles that fly near the centerline. It is found that with optimum suspension mass flow rate, in general, almost all particles flying near the centerline are melted and reach high temperature. Furthermore, the effect of angle of suspension injection is studied. One can find that angles toward the gun give more penetration of suspension in the plasma plume, resulting in better melting and higher speed of particles. Finally, particle temperature, velocity and size distributions are studied at different standoff distances with respect to the plasma gun exit. It is shown that optimum standoff distance for the studied particles and plasma plume properties is between 3 to 6 cm. Less than 3 cm standoff distance, particles have no time to reach the melting point and the base liquid would not evaporate completely; and with more than 6 cm standoff distance, particles' velocity will be significantly reduced. It should be mentioned that trajectory and penetration of suspension completely depends on velocity of suspension on one hand, and on the other hand temperature and velocity of the plasma plume. It is clear that for each condition, mass flow rate and velocity of plasma, the related modeling should be done to find velocity and temperature of particles.

ACKNOWLEDGEMENTS

This research has been done under the supervision of Dr. Wüthrich and Dr. Dolatabadi, without whose help and support this research would not be possible. Their advice and motivation was highly constructive.

This work is dedicated to my wife and my parents,
for their love and moral support.

Contents

Table of Figures

Chapter 1

Chapter 2

Chapter 3

Chapter 4

1. INTRODUCTION

This chapter covers

In this chapter an introduction to thermal spraying will be covered. In addition, plasma spraying will be discussed in detail, and finally the benefits of modeling of this Process will be argued.

1.1. Thermal spray technology

Thermal spraying techniques are coating processes in which molten or semi-molten materials coat a surface [1]. The material as a powder, suspension or solution can be injected radially or axially in flame or Plasma. A wide range of materials can be used to coat various ranges of substrates, for example, metallic powders such as nickel, aluminum, titanium and copper. In addition, non-metallic materials such as ceramics, oxides, polymers and glass can be sprayed in a wide range of sizes to coat on different substrates. It should be mentioned that there are other forms of feed-stocks like wire or ceramic rods [1].

Thermal spraying has various applications in industries especially when coated devices are subject to corrosion, erosion or overheating. It is extremely effective in increasing components' life, decreasing machinery down-time and improving performance in a wide variety of applications [1]. The heat treatment is done simultaneously, which leads to an increase in the materials' strength. It is used to recover blades of turbines, to repair critical components by coating the corroded parts which enables them to be brought back to their original size and condition. Aerospace, automotive and power generation are industries for which thermal spraying has a wide range of applications.

Although there exists several variations of thermal spray processes, the focus of this thesis is on plasma spraying technique as one of the most used techniques in various industries due its versatile and rather inexpensive characteristics compared to HVOF and cold spray systems.

1.2. Plasma spray process

Plasma spraying is one kind of thermal spraying and can be divided into two major categories; Vacuum Plasma Spraying (VPS) and Atmospheric Plasma Spraying (APS) [1]. As APS offers more flexibility for a wider range of surfaces, the thesis addresses various features of this process. Figure 1.1[1] shows a schematic of a typical APS [1]. In this process, a large heat source of plasma gun results in the ionization of the carrier gas. It is important to notice that, in plasma spraying, the temperature of gas flow is much higher in comparison to other methods of thermal spray coatings (12,000 K to 20,000 K, around 14,000 K in this study). Moreover, the velocity is more than 1000m/s (in this study about 1600 m/s), and since the temperature is high, the speed of sound will be high and it results in a Mach number of less than one (i.e. subsonic flow) in most of plasma spraying systems.

[1] Extracted from http://www.fst.nl/plasma-spray

Coating particles are injected radially or axially into the high temperature and high velocity plasma plume. Due to the high temperature of plasma gas it can melt almost all materials if the particle residence time is long enough. As mentioned above, one of the main goals in thermal sparing is to keep deposition rate in acceptable margin. The particles which are injected in to the plasma flow should have more than 300 K difference between melting point and vaporization or decomposition temperature [2]. The deposition efficiency of this process depends on various parameters but usually it is less than 60% [3]. It should be mentioned that size distribution of coating particles plays an undeniable role in the process deposition efficiency. Using fine particles will result in finer coating microstructure, however, injection of sub-micron or nano-sized particles is very challenging as particles agglomerate which results in the blockage of the powder feeder. One of the proposed solutions to this technological challenge is to suspend sub-micron and nano-particles in a base liquid and inject liquid feedstock to a conventional plasma spray gun, which is so called suspension plasma spray.

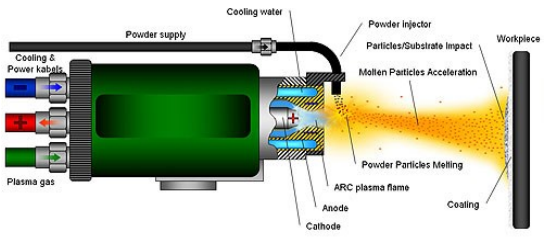

Figure 1.1 Plasma spraying system

Suspension plasma spraying (SPS) opened a new chapter in coating process with enhanced characteristics. The suspension carrying sub-micron up to few micron sized particles is radially or axially injected into a plasma plume. Understanding the trajectory, velocity, and temperature of these small particles upon impacting on the substrate is a key factor to produce repeatable and controllable coatings. The most important parameters in the SPS technique that have key influences on the coating properties are the operating condition of the torch, the fluctuations of the arc root, the primary droplet size distribution, the droplet breakup and vaporization, the melting and acceleration of the particles [4].

As mentioned above, suspension can be injected either radially or axially. In this study the suspension is injected radially as schematically shown in Figure 1.2. Suspension jet breaks up into droplets in the size range of 10-100 μm shortly after the injection to the plasma plume. As the time scale associated with the atomization is much smaller than that of evaporation process, Fazilleau et al. [4] revealed that the plasma plume atomizes the suspension before the vaporization process of the droplets becomes dominant. It is important to mention that axial and vertical distance and angle of suspension injector play a key role in penetration of suspension into the plume and has an undeniable effect on trajectory, velocity, and temperature of coating particles.

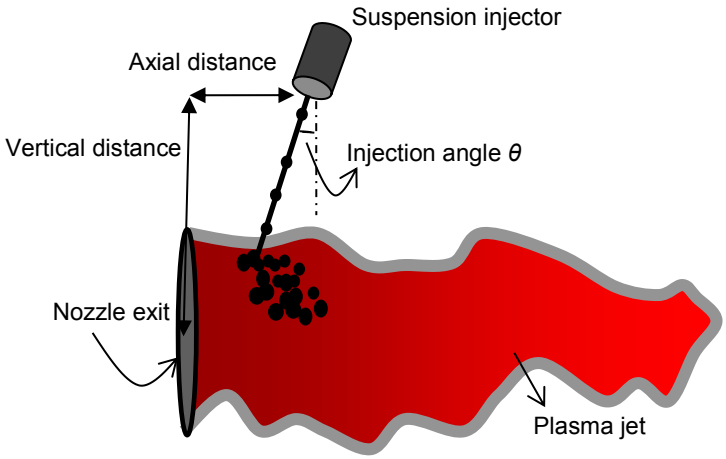

Figure 1.2 Schematic of a radial SPS

1.3. Previous works

Many simulations and experiments have been done to reveal the complex flow of thermal spray processes. Various Computational Fluid Dynamic (CFD) simulations are performed primarily to predict the plasma flow characteristics such as velocity, temperature, density and pressure fields [4 to 11]. In the next step, the focus shifted to particle injection and after that deformation of particle during the impact on the substrate. Spray nozzle configurations, different types of coating materials, and metallurgical properties of the coated material are studied in the final step.

As mentioned above, the first step is the simulation of plasma flow which can be modeled either from the inner part of the gun, or properties of the gas exiting the plasma gun can be given as inlet boundary conditions to the computational domain outside the nozzle. These two approaches are different, it is clear that the first one is more rigorous since it models the details of plasma flow (i.e. ions and electron are considered). It should be mentioned that electron temperature and velocity is higher than ions temperature and velocity and there is shear between layers of plasma. Trelles et al. [5] modeled plasma flow as non local thermal equilibrium (NLTE), they considered the presence of electron, and they used Large Eddie Simulation (LES) turbulence model while near the walls the LES model is switched to RANS to give more realistic results. On the other hand, the second approach i.e. local thermal equilibrium (LTE) is less time consuming and gives acceptable result in terms of the effect of plasma flow on injected particles.

Bolot et al. published several works on the modeling of free plasma jets with LTE assumption; they compared the results obtained from PHOENICS and Fluent solvers [6], and validated their results against experimental results [7]. Providing some key advice for the modeling of plasma jets using Fluent [8], they developed a user defined function (UDF) to correct the results of k-ε (as k-ε underestimates the length of high temperature zone). In the UDF they added a sink term to

control the rate of production of k, and consequently the k-ε model can predict more accurately the length of the high-temperature zone. They also acknowledged that the Reynolds stress model (RSM) results predict the core length correctly. In addition to commercial software, some other codes have been developed to model plasma flow. Ramshaw et al. [9] developed LAVA code to predict ionization, dissociation and recombination features of plasma flow. Flow was assumed to be steady state and 2D axisymmetric using k-ε turbulence mode to predict turbulence behavior of flow [9].

As mentioned above, the main goal/product of plasma spraying is the resultant coating which is formed by the impact and deposition of individual particles. The sprayed coatings properties strongly depend on size, velocity, and temperature of in-flight particles [1]. In plasma spraying, the particle velocity and temperature depends on the plasma plume characteristics and the penetration of the particles or suspension in the plume as well as the particle size. In typical atmospheric plasma spraying, micron-sized particles (usually 20-90 μm) are conventionally used [1] to obtain microstructured coatings. Many researchers have recently shown interest in the suspension of fine (nano- or submicron-sized) particles, or the solution of liquid precursors spraying techniques [1]. In the liquid precursors spraying technique, the reaction of solution because due to existence of a flame or jet causes fine particles to form,

although in the suspension technique, powder particles suspended in a base liquid are used [1]. Another challenging issue in APS, which can be addressed in SPS, is the negative effect of carrier gas on plasma flow in order to increase the penetration of particles. An increase in carrier gas flow rate results in poor coating [12]. Using liquid feedstock can facilitate particle penetration to the plasma plume.

Although using liquid feed-stock in SPS process provides enhanced characteristics and can solve the particle penetration problems in APS, suspension preparation and injection has its own technological challenges. The suspension is usually prepared with solid particle size of 100 nm to few microns using surfactants and ultrasound probe technique, and the base fluids are usually water, ethanol or mixture of the two [4]. However, there are some practical difficulties; for example, nano-sized particles get diverted in the stagnation zone (particularly for the convex substrate) and may not be deposited because they almost track the gas phase streamlines [13]. Moreover, preparing the suspension with nearly no particle agglomeration and sedimentation is another issue [17]. In addition, nanofluid thermal conductivity and other properties strongly depend on particle volume concentration, particle material and particle size, base fluid material (e.g., liquid hydrophilicity [15], temperature, surfactant types, and pH [14]). For example, Tanvir and Qiao [16] showed that

for n-decane+0.1 wt.% Al, as the volume fraction of surfactant (Sorbitanoleate) increases, the surface tension decreases. Many properties of nanofluids are not well understood today [14, 16]. The next step after preparation of suspension is injection of suspension.

In the suspension plasma spraying technique, suspension can be injected radially or axially [4]. Fazilleau et al. [4] revealed that the plasma plume atomizes the suspension before starting of the vaporization process of the droplets; and Melliot et al. [17] highlighted that fluctuations and instability of the plasma core play an important role in SPS specially in the case of suspension radial injection. Melliot et al. [17] categorized three types of plumes as steady, take-over and restrike. In steady mode only pure argon with high arc current intensity is used, and the fluctuations are negligible. In take-over mode, quasi-periodic motion of arc is found, and the current is not too high where argon and helium are used as the working gases. The restrike mode is completely unstable. This mode is achieved when diatomic gas mixtures such as argon/hydrogen are used and medium arc current intensity is utilized [17]. The next step will be breakup and atomization of suspension.

As mentioned, the most important parameters in the SPS technique that have key a influence on the coating properties are operating conditions of the torch, the

fluctuations of the arc root, the droplet size, the droplet breakup and vaporization and finally the melting and acceleration of the particles [4]. Fazilleau et al. [4] revealed that the plasma plume atomizes the suspension before the vaporization process of the droplets becomes dominant. They showed that in the plasma core the catastrophic breakup happens where both Rayleigh-Taylor and Kelvin-Helmholtz waves exist. The suspension vaporization process causes the plasma to cool down and the particles or their agglomerates to free. Then these particles will be heated up and accelerated inside the plasma jet [18].

Using Volume of Fluid (VOF) method, Vincent et al. [13] presented the numerical modeling of the penetration of continuous water jet in an Ar-H_2 plasma flow. In a following paper, they developed their model to display the primary fragmentation of the continuous water jet into large drops [14]. However, in both papers [13, 14] the thermal effect in terms of phase change on the water was not included. The mentioned team concentrated on the secondary atomization of droplets in the plasma plume in another paper [15]. Using VOF method, they modeled the first instant of the interaction of a droplet and a plasma jet [15]. Moreover, the effect of plasma jet fluctuations on breakup of liquid feedstock was studied by Marchand et al. [19, 20]. They used water and summarized that the droplet size, the relative velocity between droplets and main flow, and the droplet surface tension have a significant influence on the

penetration and breakup processes. However, the droplet evaporation was not considered in their studies [19, 20].

Shan et al. [16] used the Eulerian-Lagrangian approach to simulate the droplet breakup and collision in the solution precursor plasma spraying. They applied the RNG k-ε, Taylor analogy breakup (TAB), and O'Rourke's models to simulate the gas flow, the droplet breakup, and the droplet collision, respectively. They concluded that the droplet collision causes the average droplet size of the spray to increase and the droplet breakup results in the reduction of the average droplet size of the spray. Based on their results, both droplet collision and breakup should be considered in the simulation [16].

Eulerian-Lagrangian or discrete phase modeling (DPM) is used in this study to model velocity, temperature and trajectory of the droplet/particle phase. The suspension properties undergo significant changes from the injection point to the landing location due to the atomization, heat and mass transfer as well as evaporation.

These phenomena have been recently studied using DPM, especially in the high velocity suspension flame spraying (HVSFS) process [17, 21]. The novelty of this work is to use a two-component mixture model for simulating the nickel suspension with a given concentration (in this study a concentration of 15wt% is

used). The first fluid is the base liquid (ethanol), and the second fluid includes nickel properties such as density, evaporation temperature, and latent heat of evaporation.

As mentioned above, although there exists few detailed studies of various stages of suspension breakup, there are needs for further investigations of suspension atomization and capturing of the whole droplet/particle trajectories due to the complexity of this phenomenon. In the current work, with some simplifications, trajectory, velocity, and temperature of radially injected suspension into the plasma plume are simulated.

1.4. Objectives

This study is mainly driven by the great interest to enhance electrocatalytic performance of nickel electrodes using suspension plasma spraying of nickel particles [22]. Nickel particles are usually used to produce porous electrodes which are very suitable for hydrogen evolution process [23]. Nickel powder particles with ethanol as the base fluid are injected radially into the jet of a Sulzer 3MB plasma gun (the details of experimental setup with all the main parameters are explained in [22]). The suspension penetration, atomization, and evaporation

of the base liquid are numerically studied via modeling the droplet/particle trajectory, velocity, and temperature. The effects of jet momentum, axial position and injection angle on the penetration and trajectory of particles are analyzed. Moreover, the resultant particle size, velocity, and temperature distributions are investigated.

Therefore, the objectives of this work can be summarized as follows.

1 - Three dimensional modeling and simulation of plasma spray system with radial suspension injection.

2- Comparing two turbulence models; k-ε and RSM.

3 - Comparing two breakup models; Taylor Analogy Breakup (TAB) and Kelvin Helmholtz-Rayleigh Taylor (KHRT).

4 – Analyzing the effect of suspension injection on the main plasma flow for various flow rates and injection configurations.

5 – Proposing optimum operating conditions for suspension injection using the above analyses.

2. METHODOLOGY

In this chapter

An overview on the governing equations for both the main flow and the discrete phase will be presented. In addition, the physical models incorporated to model the turbulence will be discussed. Finally, break-up models that are used in this work will be presented.

2.1. Numerical modeling

Modeling of plasma spraying process is very helpful in order to gain a better understanding of the physics governing this process and to reduce the amount of trial and error in experiments. For instance, to find the optimum angle and position of the injector, it is easier to use numerical modeling. To model the phenomenon we should know which gases are used in the process, which of them have major a role, and then the thermodynamic properties in working temperature that should be given to the CFD solver. In this study the primary gas is argon. Generally, hydrogen and helium will be used as secondary gases, but in this work, because we needed more stability in the plasma flow, only pure argon is utilized.

2.2. Significant assumptions of this work

In this work suspension of nickel particles in ethyl alcohol (ethanol) is injected in a plasma plume. As described by Bolos et al. [24] it is assumed that the plasma flow is at local thermal equilibrium (LTE). The second assumption is that the plasma flow has the ideal gas and temperature-dependent thermodynamic and transport properties, following Remesh et al. [12]. By these assumptions the presence of ions and electrons in the plasma are neglected; while the macroscopic changes of fluid properties due to ionization and

dissociation are taken into account. It should be mentioned that in non-LTE plasma modeling the shear between layers of plasma is modeled. In reality there is shear between layers of plasma because the speed and temperature of electrons is more than that of ions. However, since the mass of electrons is very low in comparison to ions, their effect is negligible. In other words, the momentum that one electron can transfer during its impact with particles, droplets or surrounding gas can be considered to be negligible.

2.3. Governing equations

2.3.1. The mass conservation equation

The mass conservation equation is as follows:

$$\frac{\partial \rho}{\partial t} + \nabla \cdot \left(\rho \vec{u} \right) = 0 \qquad (2\text{-}1)$$

Equation 2-1 is the general form for mass conservation or continuity and can be used for incompressible and compressible flows. It should be mentioned that our case is compressible. Moreover, since our case is steady the first term on the left-hand side of the equation will be zero.

2.3.2. The momentum conservation equation

The momentum conservation equation in an inertial frame of reference is

$$\frac{\partial}{\partial t}(\rho \vec{u}) + \nabla \cdot (\rho \vec{u}\,\vec{u}) = -\nabla p + \nabla \cdot \overline{\overline{\tau_{eff}}} \tag{2-2}$$

In equation (2-2) p is the static pressure and $\overline{\overline{\tau_{eff}}}$ is the tensor of stress, defined as

$$\overline{\overline{\tau_{eff}}} = \mu_{eff}\left[\left(\nabla \vec{u} + \nabla \vec{u}^{\mathrm{T}}\right) - \frac{2}{3}\nabla \cdot \vec{u} I\right] \tag{2-3}$$

In the above equation μ_{eff} is the effective viscosity ($\mu+\mu_t$, and μ_t is the turbulent viscosity, defined according to the turbulence model, and in this work k-ε or RSM), and I is the unit tensor. Moreover, the second term on the right-hand side of equation is the volume dilatation which accounts for the changes in the volume [25]. Moreover, since our case is steady the first term on the left-hand side of the equation will be zero.

2.3.3. The energy equation

The energy equation will be in the following form.

$$\frac{\partial}{\partial t}(\rho E) + \nabla \cdot (\vec{u}(\rho E + p)) = \nabla \cdot \left(k_{eff} \nabla T + \overline{\overline{\tau_{eff}}} \cdot \vec{u}\right) \tag{2-4}$$

If k_{eff} represents the effective conductivity (defined similar to the effective viscosity) and the first part of the right-hand side shows energy transfer due to conduction, the second one represents this transfer due to viscous dissipation.

Moreover, since our case is steady the first term on the left-hand side of the equation will be zero [25].

In Equation 2-4, E is defined as follows.

$$E = h - \frac{p}{\rho} + \frac{u^2}{2} \tag{2-5}$$

2.3.4. Equation of state

The ideal gas equation of state is used not only to close the system of the equation but also take into account the effect of compressibility.

$$p = \rho R_g T \tag{2-6}$$

2.3.5. Species transport equation

When the conservation equation for a chemical species is solved, a local mass fraction for each species should be predicted, Y_i, to solve the convection-diffusion equation for each species. This equation takes the following general form.

$$\frac{\partial}{\partial t}(\rho Y_i) + \nabla . (\rho \vec{v} Y_i) = -\nabla . \vec{J_\iota} + R_i + S_i \tag{2-7}$$

where R_i is rate of production of species i by chemical reaction, which is zero in our case since there is no reaction (no flame). S_i is the rate of creation by adding

from the dispersed phase or any user-defined function. This equation should be solved for N-1 species where n is the number of total species. When the mass fraction of all species is unity, the mass fraction of the N*th* species can be defined as 1- N [25]. In addition, it is clear that the first term on the left-hand side is zero since our model is steady.

2.4. Geometry and boundary conditions

The geometry and boundary conditions are shown in Figure 2.1. As the physical geometry is symmetric with respect to the vertical plane, only half of the physical domain is modeled using symmetric boundary condition for the vertical plane. The plasma nozzle has a circular cross section with a diameter of 7.88 mm entering the computational domain as "velocity inlet" boundary. The computational domain diameter is 66 mm with a length of 90 mm in front of the nozzle and 10 mm towards the back of the nozzle. Suspension injector is located at 17mm from the plasma gun exit plane and 25mm from the centerline. As shown in Figure 2.1, a pressure-outlet type of boundary is used on the periphery. To model the nozzle inlet velocity, an inlet type of boundary is utilized as it gives better convergence in comparison to a mass flow inlet or pressure-inlet boundary. To cover the mass flow that is used in the experiment, a velocity

profile should be used for the inlet. To give this profile to Fluent a user-defined function (UDF) is written. The velocity profile is given as Equation 2-8 [26, 27, 28].

$$v = v_0[\,1 - \left(\frac{r}{R_0}\right)^{n_v}] \tag{2-8}$$

where n_v=2 and v_0=1800 m/s [26, 27]. The temperature profile is assumed to be uniform and equal to 12,250 K.

The turbulence intensity at the inlet boundary is set to 2% [20]. Turbulence intensity is defined as $\frac{\acute{u}}{\bar{u}}$ where $\acute{u}$ is the root-mean-square of the turbulent velocity fluctuations and $\bar{u}$ is the mean velocity [25].

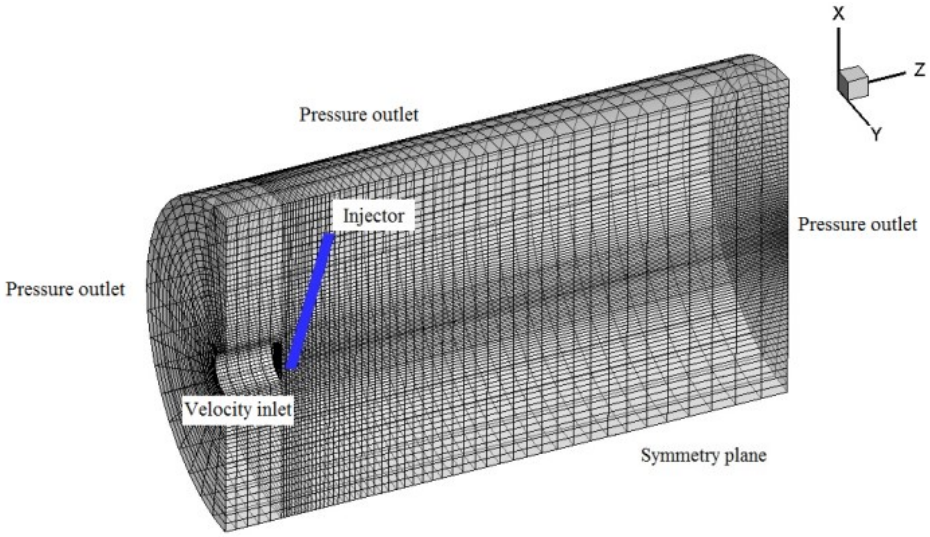

Figure 2.1 Geometry and boundary conditions [11]

2.5. Numerical techniques

2.5.1. Turbulence model

Two turbulence models of $k-\varepsilon$ and RSM are studied in this work and their results are compared with experimental and other numerical studies. In the following paragraphs, the *Reynolds* averaging method will be discussed, and then the formulation of $k-\varepsilon$, and finally the RSM will be argued.

In *Reynolds* averaging, the solution variables from the exact Navier-Stokes equations are decomposed into a fluctuating term and a time or ensemble averaged term; for example, the velocity component can be expressed as,

$$\vec{u} = \bar{\vec{u}} + \vec{u}' \tag{2-9}$$

where $\vec{u}'$ and $\bar{\vec{u}}$ are the fluctuating and mean components, respectively [25]. Variables should be substituted into the instantaneous continuity and momentum equations, yielding:

$$\frac{\partial}{\partial t}(\rho) + \nabla \cdot (\rho \vec{u}) = 0 \tag{2-10}$$

and

$$\frac{\partial}{\partial t}(\rho \vec{u}) + \nabla \cdot (\rho \vec{u}\,\vec{u}) = -\nabla p + \nabla \cdot \bar{\bar{\tau}} + \nabla \cdot \left(-\rho \overline{\vec{u}'\vec{u}'}\right) \tag{2-11}$$

where the stress tensor is expressed as

$$\bar{\bar{\tau}} = \mu\left[\left(\nabla \vec{u} + \nabla \vec{u}^{\mathrm{T}}\right) - \frac{2}{3}\nabla \cdot \vec{u} I\right] \tag{2-12}$$

- $\frac{\partial}{\partial t}(\rho \vec{u})$ is the unsteady term
- $\nabla \cdot (\rho \vec{u} \vec{u})$ is the advection term
- ∇p is the pressure gradient
- $\left(-\rho \overline{\vec{u}' \vec{u}'}\right)$ is the Reynolds shear stress
- $\nabla \cdot \overline{\overline{\tau}}$ is the diffusion term
- I is the identity matrix.

Equation 2.11 is called the *Reynolds Averaged Navier-Stokes (RANS)* equations [25]. The *Reynolds* stress term, $-\rho \overline{\vec{u}' \vec{u}'}$, should be appropriately modeled to close the system of equations. Hence, the first step of closure based on Boussinesq's hypothesis is relating the *Reynolds* stresses to the mean velocity gradients.

$$-\rho \overline{u_i' u_j'} = \mu_t \left(\frac{\partial u_i}{\partial x_j} + \frac{\partial u_j}{\partial x_i} \right) - \frac{2}{3} \left(\rho k + \frac{\partial u_k}{\partial x_k} \right) \delta_{ij} \tag{2-13}$$

where k is turbulence kinetic energy, μ_t is turbulent viscosity, and δ is Dirac delta function [25].

The relatively low computational cost is the advantage of this approach. μ_t is computed as a function of k and ε and two additional transport equations should be solved; the first one for the turbulence kinetic energy, k, and the second one for the turbulence dissipation rate, ε. The disadvantage of Boussinesq's

hypothesis is that it assumes μ_t as an isotropic scalar quantity, which is not strictly true for all conditions [25].

The standard $k-\varepsilon$ model proposed by Launder and Spalding [29] is known to be slightly over-diffusive in certain situations.

$$\frac{\partial}{\partial t}(\rho k)+\frac{\partial}{\partial x_i}(\rho k u_i)=\frac{\partial}{\partial x_j}\left[\left(\mu+\frac{\mu_t}{\sigma_k}\right)\frac{\partial k}{\partial x_j}\right]+G_k+G_b-\rho\epsilon-Y_M+S_k \quad (2\text{-}14)$$

$$\frac{\partial}{\partial t}(\rho \epsilon)+\frac{\partial}{\partial x_i}(\rho \epsilon u_i)=\frac{\partial}{\partial x_j}\left[\left(\mu+\frac{\mu_t}{\sigma_\epsilon}\right)\frac{\partial \epsilon}{\partial x_j}\right]+C_{1\epsilon}\frac{\epsilon}{k}(G_k+C_{3\epsilon}G_b)-C_{2\epsilon}\rho\frac{\epsilon^2}{k}+S_\epsilon \quad (2\text{-}15)$$

where

$\mu_t = C_\mu \rho \frac{k^2}{\epsilon}$, C_μ is an empirical constant and usually is considered to be 0.09, and G_k represents the generation of turbulence kinetic energy due to the mean velocity gradients [25]. This part is overestimated in our modeling and gave low penetration of plasma into the domain. Thus another model is used (RSM model), which will be further discussed in this chapter.

$$G_k = \mu_t S^2 \quad (2\text{-}16)$$

where S is the modulus of the mean rate-of-strain tensor, defined as

$$S = \sqrt{2 S_{ij} S_{ij}} \quad (2\text{-}17)$$

G_b is the generation of turbulence kinetic energy due to buoyancy, which is zero in our case since buoyancy do not playing a significant role.

$Y_M = 2\rho\epsilon M_t^2$, Y_M is the contribution of dilatation of fluctuating in compressible turbulence to the dissipation rate, where M_t is the turbulent Mach number, defined as,

$$M_t = \sqrt{\frac{k}{a^2}} \tag{2-18}$$

and a is the speed of sound.

For the standard and realizable k-ε models, the effective thermal conductivity is given by [25],

$$k_{eff} = k + \frac{c_p \mu_t}{Pr_t} \tag{2-19}$$

where

- $C_{1\epsilon}$, $C_{2\epsilon}$, $C_{3\epsilon}$ are constants
- σ_k , σ_ϵ are the turbulent Prandtl numbers for k and ε, respectively
- S_k , S_ϵ are user-defined source terms
- $\frac{\partial}{\partial t}(\rho k)$ is the local rate of change of the average turbulence kinetic energy
- $\frac{\partial}{\partial x_i}(\rho k u_i)$ is the change of k due to advection. The sum of this term with the previous one is the substantial derivative of k, which gives the rate of change of k following a fluid.

Reynolds stress model (RSM)

Since a round jet of plasma is to be modeled with high speed and abrupt change in shear stress and temperature, the RSM model will be applied to model a round jet of plasma [30]. The RSM is very time-consuming in comparison to *k*-*ε* and quite difficult to have convergence; on the other hand, it will give more accuracy as it is not as dissipative as *k*-*ε* model. To have better convergence it is recommended to start with *k*-*ε*, and after the convergence the solver should be switched to RSM. The Reynolds-averaged Navier-Stokes equations are closed by solving the transport equations for the Reynolds stress, together with an equation for the dissipation rate in the RSM model, which means that in three dimensions seven additional transport equations must be solved. In Reynolds average method the variables of the exact Navier-Stokes equations should be decomposed into a time- or ensemble-averaged term, and a fluctuating term. The velocity component can be expressed as,

$$\vec{u} = \bar{\vec{u}} + \vec{u}' \tag{2-20}$$

$$\underbrace{\frac{\partial}{\partial t}\left(\rho\overline{u_i'u_j'}\right)}_{1}+\underbrace{\frac{\partial}{\partial x_k}\left(\rho u_k\overline{u_i'u_j'}\right)}_{2}=\underbrace{-\frac{\partial}{\partial x_k}\left(\rho\overline{u_i'u_j'u_k'}+\overline{p\left(\delta_{kj}u_i'+\delta_{ik}u_j'\right)}\right)}_{3}$$
$$+\underbrace{\frac{\partial}{\partial x_k}\left(\mu\frac{\partial}{\partial x_k}\left(\overline{u_i'u_j'}\right)\right)}_{4}-\underbrace{\rho\left(\overline{u_i'u_k'}\frac{\partial u_j}{\partial x_k}+\overline{u_j'u_k'}\frac{\partial u_i}{\partial x_k}\right)}_{5} \qquad (2\text{-}21)$$
$$+\underbrace{\overline{p\left(\frac{\partial u_i'}{\partial x_j}+\frac{\partial u_j'}{\partial x_i}\right)}}_{6}-\underbrace{2\mu\left(\overline{\frac{\partial u_i'}{\partial x_k}\frac{\partial u_j'}{\partial x_k}}\right)}_{7}$$

1) $\frac{\partial}{\partial t}\left(\rho\overline{u_i'u_j'}\right)=$ Local Time Derivative

2) $\frac{\partial}{\partial x_k}\left(\rho u_k\overline{u_i'u_j'}\right)=$ Convection

3) $\frac{\partial}{\partial x_k}\left(\rho\overline{u_i'u_j'u_k'}+\overline{p\left(\delta_{kj}u_i'+\delta_{ik}u_j'\right)}\right)=$ Turbulent Diffusion

4) $\frac{\partial}{\partial x_k}\left(\mu\frac{\partial}{\partial x_k}\left(\overline{u_i'u_j'}\right)\right)=$ Molecular Diffusion

5) $\rho\left(\overline{u_i'u_k'}\frac{\partial u_j}{\partial x_k}+\overline{u_j'u_k'}\frac{\partial u_i}{\partial x_k}\right)=$ Stress Production

6) $\overline{p\left(\frac{\partial u_i'}{\partial x_j}+\frac{\partial u_j'}{\partial x_i}\right)}=$ Pressure Strain

7) $2\mu\left(\overline{\frac{\partial u_i'}{\partial x_k}\frac{\partial u_j'}{\partial x_k}}\right)=$ Dissipation

In Equation (2-21), the pressure strain [31, 32] and the turbulent diffusion terms [33] should be modeled to close the equation. The turbulent kinetic energy should be calculated by taking the trace of the Reynolds stress tensor as,

$$k = \frac{1}{2}\overline{u_i' u_i'} \tag{2-22}$$

The dissipation tensor should modeled as,

$$\varepsilon_{ij} = \frac{2}{3}\delta_{ij}\left(\rho\varepsilon + Y_M\right) \tag{2-23}$$

Here Y_M is an additional dilatation dissipation term and is defined as

$$Y_M = 2\rho\varepsilon M_t^2 \tag{2-24}$$

where the turbulent Mach number is defined as follows.

$$M_t = \sqrt{\frac{k}{a^2}} \tag{2-25}$$

In the above equation, a is the speed of sound, which is changed by temperature drastically.

The scalar dissipation rate, ε, is calculated from the following equation.

$$\frac{\partial}{\partial t}\left(\rho\varepsilon\right) + \frac{\partial}{\partial x_i}\left(\rho\varepsilon u_i\right) = \frac{\partial}{\partial x_j}\left[\left(\mu + \frac{\mu_t}{\sigma_\varepsilon}\right)\frac{\partial\varepsilon}{\partial x_j}\right] C_{\varepsilon 1}\frac{1}{2}P_{ii}\frac{\varepsilon}{k} - C_{\varepsilon 2}\rho\frac{\varepsilon^2}{k} \tag{2-26}$$

In the above equation, σ_ε = 1.0, $C_{\varepsilon 1}$ = 1.44, and $C_{\varepsilon 2}$ = 1.92. P_{ii} is the stress production term in the Reynolds stress equation.

The turbulent viscosity is computed similar to the k-ε model as,

$$\mu_t = \rho C_\mu \frac{k^2}{\varepsilon} \tag{2-27}$$

where $C_\mu = 0.09$.

2.5.2. Coupling of pressure and velocity

In this study, the flow is compressible and density is varied by temperature. Since the Mach number is not too high (gas flow is still subsonic), a pressure-based solver is utilised. The pressure-based solver is more stable and converges easier in comparison to the density-based solver.

Figure 2.2 schematically shows various steps used in the pressure-based algorithm. In this model, the program first solves the velocity field (u, v and w) and then uses a pressure correction factor to control the velocity; after this it updates the velocity parts and finally solves the other equations and updates all the variables. The convergence is achieved if all the residuals are smaller than a predefined value.

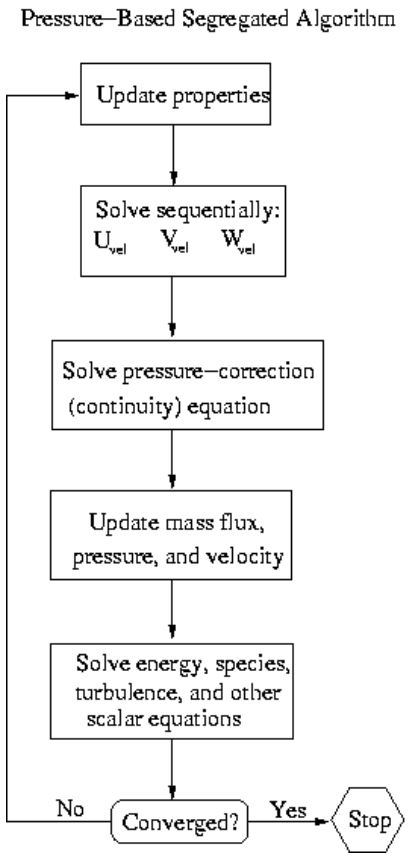

Figure 2. 2 Overview of the pressure-based solution method [25]

2.6. Eulerian-Lagrangian approach

An Eulerian-Lagrangian approach with two-way coupling method is used to model the gas flow and particle behavior using ANSYS® Fluent® release 14. The Reynolds Stress Model (RSM) is applied here to simulate the gas phase turbulence and the gas flow is assumed to be compressible. The steady mode is

considered here, so the working gas is only argon and the arc fluctuations are negligible. The gas is chemically inert and its transport and thermodynamic properties are only dependent on temperature [12]. The ideal gas model is used, and this assumption is acceptable when temperature is high enough and pressure is close to the ambient pressure [12]. In reality, plasma flow is in non-local thermal equilibrium (NLTE) [5], but local thermal equilibrium (LTE) is usually assumed for the plasma flow modeling [12, 24]. LTE is assumed in this work and NLTE remains as future work.

Discrete phase modeling is used in this study to model velocity, temperature and trajectory of the particle phase. The suspension properties undergo significant changes from the injection point to the landing location due to the atomization, heat and mass transfer as well as evaporation. The novelty of this work is to use a variable mixture model for simulating the suspension; the first fluid (ethyl-alcohol) is the base liquid, and the second fluid includes nickel properties such as density, evaporation point, and latent heat of evaporation.

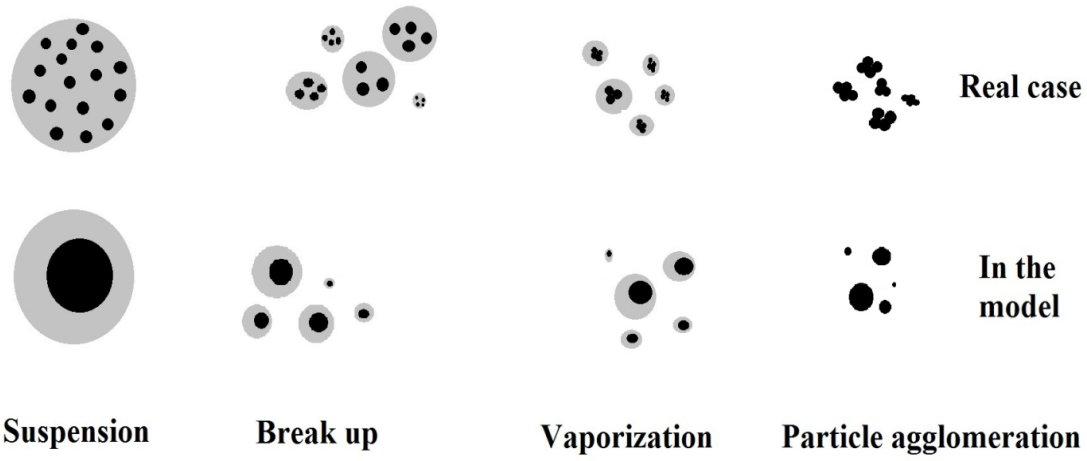

Figure 2.3 The suspension atomization, evaporation and particle agglomeration in the real and the model cases [11]

Figure 2.3 schematically shows the assumptions made in the present work. A piecewise-linear function is utilized to model surface tension. As far as breakup is dominant [4], when the suspension temperature is less than the evaporation point for alcohol, the suspension surface tension, which is around 30% more than that of pure alcohol, is used [34]. Fine droplets will be produced afterwards and the breakup processes will be stopped. However, the ethanol vaporization is still ongoing until all ethanol evaporates. Next, the surface tension of molten nickel which is very high in comparison to the suspension surface tension is utilized. The stochastic tracking model is assumed to consider the effect of turbulence fluctuations on particle trajectories [35]. The momentum

conservation equation of the suspension phase includes the drag force where the drag coefficient is as follows,

$$C_D = a_1 + \frac{a_2}{Re} + \frac{a_3}{Re^2} \tag{2-28}$$

where a_1, a_2 and a_3 are constants and Re is the Reynolds number [35]. The lumped capacity method is applied to model the suspension phase heat transfer, and the Ranz-Marshal correlation for spheres is used to obtain the Nusselt number [35]. To model the particle temperature behavior before its melting point, which is around 1728K, the specific heat of the pure solid nickel is used. The heat of fusion for nickel particles is approximated using the formula below:

$$C \, \Delta \, T = H \tag{2-29}$$

where H is the fusion heat, $\Delta \, T$ is assumed to be 10K (from 1728K to 1738K) and C is the estimated specific heat (around 29600 J/kg). After melting (for particles with a temperature more than 1738 K), the specific heat is assumed to be constant and equal to the specific heat of the pure liquid nickel until the particles' temperature reaches the evaporation point [11]. Figure 2.4 shows the specific heat variations as a function of particle temperature. Since the flow is symmetric around the X-Z plane, half of the jet is modeled (the geometry is shown in Figure 2.1).

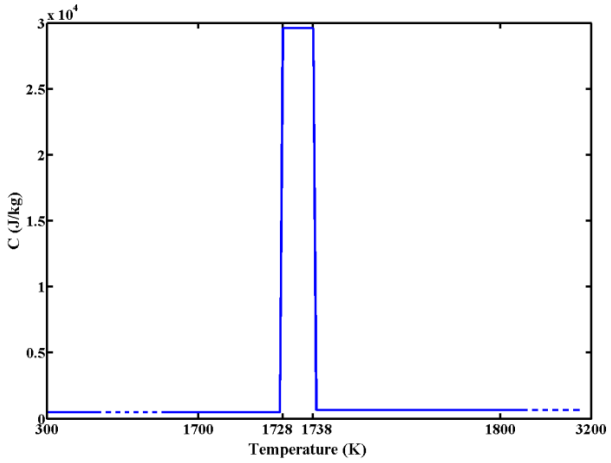

Figure 2.4 The variation of particle phase specific heat as a function of temperature [11]

2.7. Particle tracking

Transport equation is solved for continuous phase; moreover, a Lagrangian tracking approach is utilized to predict behavior of in-flight particles. Particles are assumed to be spherical and inert.

2.7.1. Particle force balance

The force balance on the particles in discrete phase should be integrated to achieve the trajectory. For X direction in the Cartesian coordinates, it is given as [25]:

$$\frac{du_p}{dt} = F_D\left(\vec{u} - \vec{u}_p\right) + \vec{F} \tag{2-30}$$

where F is an additional force term and $F_D(\vec{u} - \vec{u}_p)$ is the drag force. All forces are per unit mass of particle and F_D is as follows [25],

$$F_D = \frac{18\,\mu\, C_D Re}{\rho_p d_p^2 24} \tag{2-31}$$

In addition, the relative Reynolds number is defined as,

$$Re \equiv \frac{\rho\, d_p\, |\vec{u}_p - \vec{u}|}{\mu} \tag{2-32}$$

where $\vec{u}$ and ρ are velocity and density of gas phase, respectively; μ is molecular viscosity of gas phase; $d_p$is particle diameter; and finally, $\vec{u}_p$ and ρ_p are velocity and density of the discrete phase (suspension, droplet or particle after evaporation of base liquid). C_D is calculated as explained in Equation 2.28. It is important to mention that the gravitational force compared to the inertial force can be assumed negligible.

2.7.2. Discrete phase heat transfer

Since the particles used in a suspension spraying are relatively small in size, it can be assumed that internal resistance to heat transfer is negligible there; that is, at each step of integration the particles are at uniform temperature (Bi < 0.1). Radiation heat transfer is also assumed to be negligible. With these assumptions, the energy balance for each individual particle yields,

$$m_p c_p \frac{dT_p}{dt} = hA_p\left(T_\infty - T_p\right) \tag{2-33}$$

where m_p and A_p are the mass and the cross-sectional area of the particles, respectively. The convective heat transfer coefficient, h, is calculated using the correlation of Ranz and Marshall [36,37].

$$Nu = \frac{hD_p}{k} = 2.0 + 0.6\,\mathrm{Re}_p^{1/2}\,\mathrm{Pr}^{1/3} \tag{2-34}$$

where Pr and k are the Prandtl number and the thermal conductivity of the continuous phase, respectively.

It should be mentioned that in equation (2-26) c_p is calculated as explained in equation 2.29 and figure 2.4, to take into account the heat of fusion for Nickel.

2.7.3. Breakup models

There are two major types of breakup; primary and secondary breakup. Primary breakup happens first and secondary breakup follows.

Primary Breakup

When suspension or any fluid is injected radially in a plasma plume or any high-velocity flow, it undergoes primary breakup, and after that, secondary breakup will start. To model primary breakup, interface tracking methods such as Volume of Fluid (VOF) should be used, and for this kind of modeling, the mesh should be very fine (at least 10 cells per droplet diameter). Since our domain is very large, using this size of mesh will be very time-consuming. Therefore, primary breakup is neglected in this work. The main effect of this simplification could be less penetration of suspension in the plasma plume, which will be further discussed in the following chapter.

Secondary Breakup

The main focus in the current work is on secondary breakup, and different methods are compared. One of the most important improvements of Fluent 14 in comparison to Fluent 13 and 12 is that it offers four formulations of breakup (in the earlier versions only two methods were available).

1- Taylor Analogy Breakup (TAB) Model

2- Kelvin-Helmholtz, Rayleigh-Taylor (KHRT) Breakup Model

3- Wave Breakup Model

4- Stochastic Secondary Droplet (SSD) Model

The KHRT and SSD models are only available in the new version of ANSYS Fluent (version 14).

For the secondary breakup simulation, TAB and KHRT models are applied. TAB and KHRT models are suitable for droplets with low and high Weber numbers, respectively [25].

Taylor Analogy Breakup (TAB) Model

The classic method for calculating droplet breakup is the Taylor analogy breakup (TAB) model which is applicable to many engineering sprays. This method is based upon Taylor's analogy [25] between a spring mass system and an oscillating and distorting droplet. Table 2.1 shows the comparison between these two systems.

Table 2.1 Comparison of a Spring-Mass System to a Distorting Droplet

Spring-Mass System	**Distorting and Oscillating**
restoring force of spring	surface tension forces
external force	droplet drag force
damping force	droplet viscosity forces

Kelvin-Helmholtz, Rayleigh-Taylor (KHRT) breakup model

This method uses a combination of the effects of Kelvin-Helmholtz waves that are driven by aerodynamic forces and Rayleigh-Taylor instabilities due to acceleration of shed drops ejected into the free-stream flow. Droplet breakup is modeled by tracking wave growth on the surface of the droplet in both mechanisms. Breakup will occur due to the fastest growing instability based on local conditions.

Wave breakup model

The wave breakup model of Reitz [25] is an alternative to the TAB model. This model is appropriate for high-Weber-number flows. Breakup of the droplets is considered to be induced by the relative velocity between the liquid and gas phases. Time of breakup and the resulting droplet size in this model are assumed to be related to the fastest growing Kelvin-Helmholtz instability, derived from the jet stability analysis. Details of the newly-formed droplets are predicted by the growth rate and wavelength of this instability.

The wavelength of the fastest-growing unstable surface wave on the parent droplet is used to calculate the radius of the newly formed droplets. In other words,

$$r = B_0 \Lambda \tag{2-35}$$

where B_0 is a model constant set equal to 0.61 based on the work of Reitz [37]. Moreover, the droplet radius change in the parent parcel is given by

$$\frac{da}{dt} = -\frac{(a-r)}{\tau}, r \leq a \tag{2-36}$$

where the breakup time, τ, is given by,

$$\tau = \frac{3.726\, B_1 a}{\Lambda \Omega} \tag{2-37}$$

where Λ and Ω are calculated from the following equation.

$$\frac{\Lambda}{a} = 9.02 \frac{\left(1+0.45Oh^{0.5}\right)(1+0.4Ta^{0.7})}{(1+0.87We_2^{1.67})^{0.6}} \tag{2-38}$$

$$\Omega\left(\frac{\rho_1 a^3}{\sigma}\right) = \frac{(0.34+0.38We_2^{1.5})}{(1+Oh)(1+1.4Ta^{0.6})} \tag{2-39}$$

where *Oh* and *Ta* are the Ohnesorge and Taylor numbers given by equation 2-40 and 2-41.

$$Oh = \sqrt{We_1}\Big/ Re_1 \tag{2-40}$$

$$Ta = Oh\sqrt{We_2} \tag{2-41}$$

where We_1 and We_2 are the liquid and gas Weber numbers, respectively, given by equation 2-42 and 2-43.

$$We_1 = \rho_1 U^2 \frac{a}{\sigma} \tag{2-42}$$

$$We_2 = \rho_2 U^2 \frac{a}{\sigma} \tag{2-43}$$

In addition, equation (2-44) describes the Reynolds number [25].

$$Re_1 = U \, {}^{a}/_{\nu_1} \tag{2-44}$$

Rayleigh-Taylor breakup model

The Rayleigh-Taylor (RT) model is based on wave instabilities on the droplet surface, like the Kelvin-Helmholtz model. The fastest growing wave frequency is computed by,

$$\Omega_{RT} = \sqrt{\frac{2\left(-g_t\left(\rho_p - \rho_g\right)\right)^{\frac{3}{2}}}{3\sqrt{3\sigma}\left(\rho_p - \rho_g\right)}} \tag{2-45}$$

where g_t is the acceleration of droplet in the direction of the droplet travel. The wave number is calculated by

$$K_{RT} = \sqrt{\frac{-g_t\left(\rho_p - \rho_g\right)}{3\sigma}} \tag{2-46}$$

When RT waves have been growing for a time greater than the breakup time, τ_{RT}, the breakup occurs.

Here τ_{RT} is

$$\tau_{RT} = \frac{C_\tau}{\Omega_{RT}} \tag{2-47}$$

While the diameter is greater than the predicted wave length $2\pi\left(C_{RT}/K_{RT}\right)$ corresponding to the fastest wave growth rate, the wave growth is tracked. The radius of local child droplets is calculated with

$$r_c = \frac{\pi\, C_{RT}}{K_{RT}} \tag{2-48}$$

3. RESULTS AND DISCUSSION

In this chapter

In this chapter, numeric results of modeling of plasma flow without any injection obtained with two turbulence models are compared. After validation of these results, results of two breakup models are compared. Finally the optimum injection position and condition are determined.

3.1. Introductions

As a first step in this chapter, plasma flow without any suspension will be studied. The temperature profile is compared to other numerical and experimental results. After validating the temperature profile, seven cases of injection will be studied. Finally, the optimum position for the substrate based on the predicted particle size, temperature and velocity distributions will be discussed. For more convenience, all cases studied are named in table 3.1.

Table 3.1 Detail information for each case study

Case number	Suspension Flow rate (gr/s)	Injection Velocity (m/s)	Nozzle position (mm from plasma gun)	Nozzle angle	Break-up Model
Case 1	0.23	V=12.9	7	14°	KHRT
Case 2	0. 45	V=25.7	7	14°	KHRT
Case 3	0.68	V=38.6	7	14°	KHRT
Case 4	0.45	V=25.7	1	0°	KHRT
Case 5	0.45	V=25.7	17	14°	KHRT
Case 6	0.45	V=25.7	7	14°	TAB
Case 7	0.45	V=12.9	7	14°	TAB

3.1 Gas flow

As mentioned before, the first step before the suspension injection is validating the results of the gas flow (plasma plume). Figure 3.1 shows the centerline temperature profiles of the gas phase obtained by RSM and *k-ε* models. As can be seen from the figure, the RSM solver produces more realistic

results for modeling of the high-temperature region in the plasma jet and it has better agreement with the numerical and experimental results in the literature [6, 39]. It should be mentioned that the RSM model is more time-consuming and more difficult to obtain convergence. However, as is it clear in Figure 3.1, *k-ε* model significantly underestimates the length of the high-temperature zone which affects the temperature of the injected droplets/particles. For example, at 2cm from the nozzle, *k-ε* models gave a temperature of 4000 K, while RSM gave more than 10,000 k. As mentioned in the methodology chapter, this underestimation is due to abrupt change in shear stress and temperature. It should be mentioned that same geometry and boundary conditions as used in Bolot et al. [6] work is utilized to validate the RSM model results.

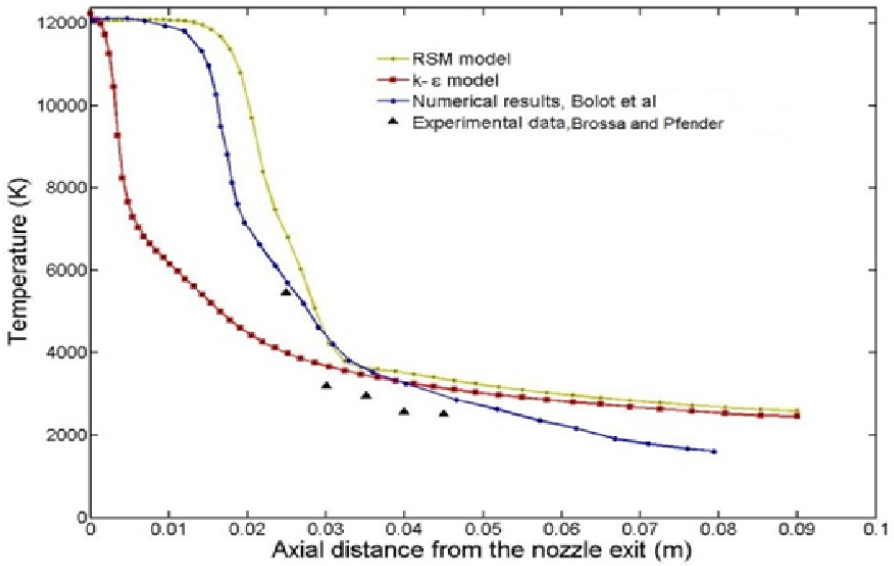

Figure 3.1 Centerline temperature profiles obtained by RSM and *k-ε* models compared with experimental [6] and numerical data [38]

Figure 3.2 shows the temperature contours obtained with (a) *k-ε* and (b) RSM. As discussed, the RSM result is more realistic. In addition Figure 3.3 shows velocity contours obtained with these two methods.

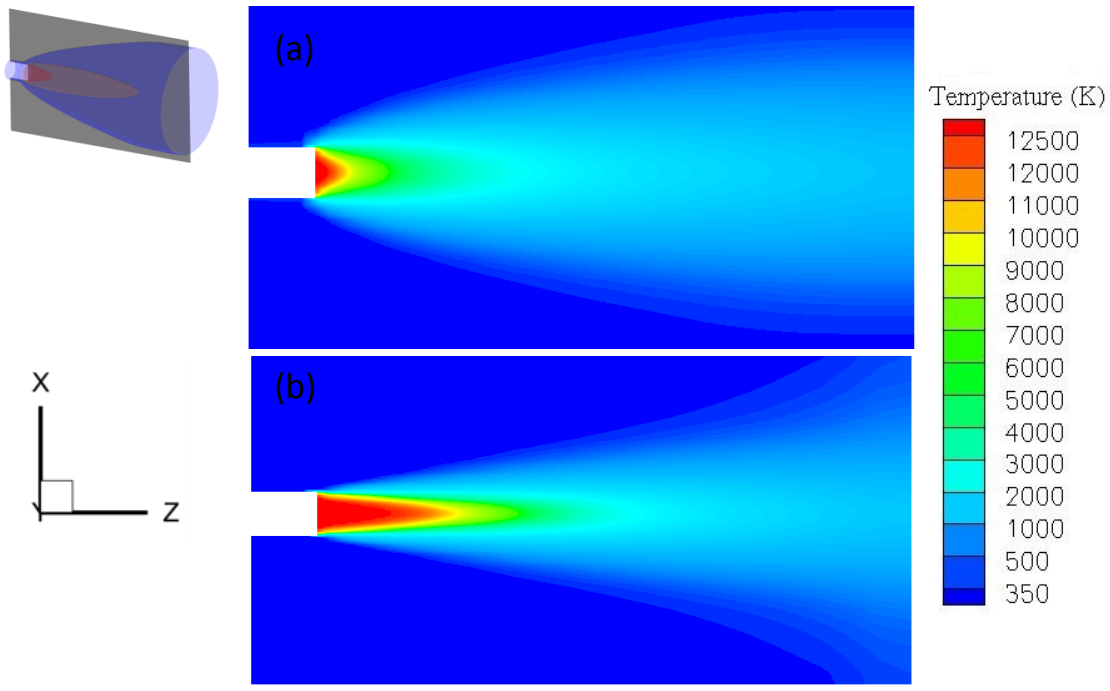

Figure 3.2 Temperature contours obtained by (a) *k-ε* and (b) RSM models

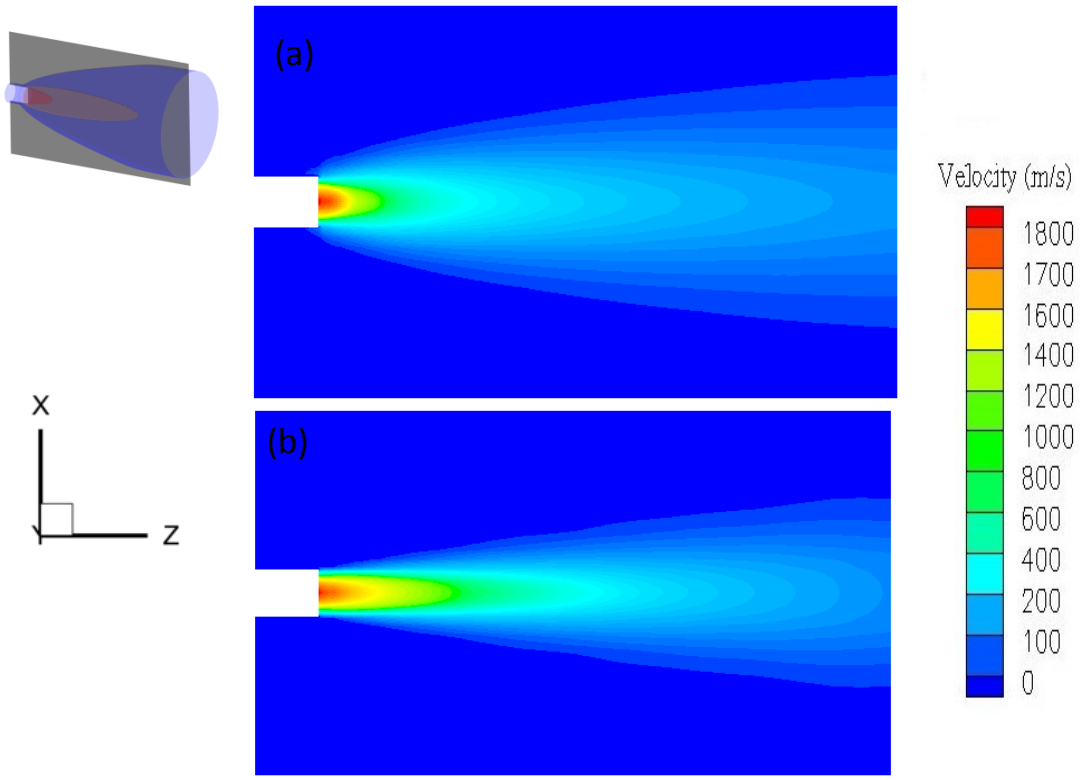

Figure 3. 3 Velocity contours obtained by (a) *k-ε* and (b) RSM models

As the gas flow simulation results obtained by *k-ε* model unrealistically underestimates the temperature field, in the rest of this study the RSM model coupled with the discrete phase is utilized.

3.2. Two-way coupled gas-particulate flow

After studying temperature and velocity of the plasma plume, the effect of suspension injection on the plume is studied. Figure 3.4 shows the effect of the suspension mass flow rate on the gas phase velocities when the suspension mass flow rate increases from 0.23 g/s (case 1) to 0.45 g/s (case 2) and finally 0.68 g/s

(case 3). As can be seen, as the suspension mass flow rate increases (so the momentum force increases), the penetration in the plasma plume grows and the gas phase velocity in this region decreases. This figure is obtained using KHRT and RSM models.. On the right side of Figure 3.4, Y-Z plane, is the perpendicular plane to the symmetry plane.

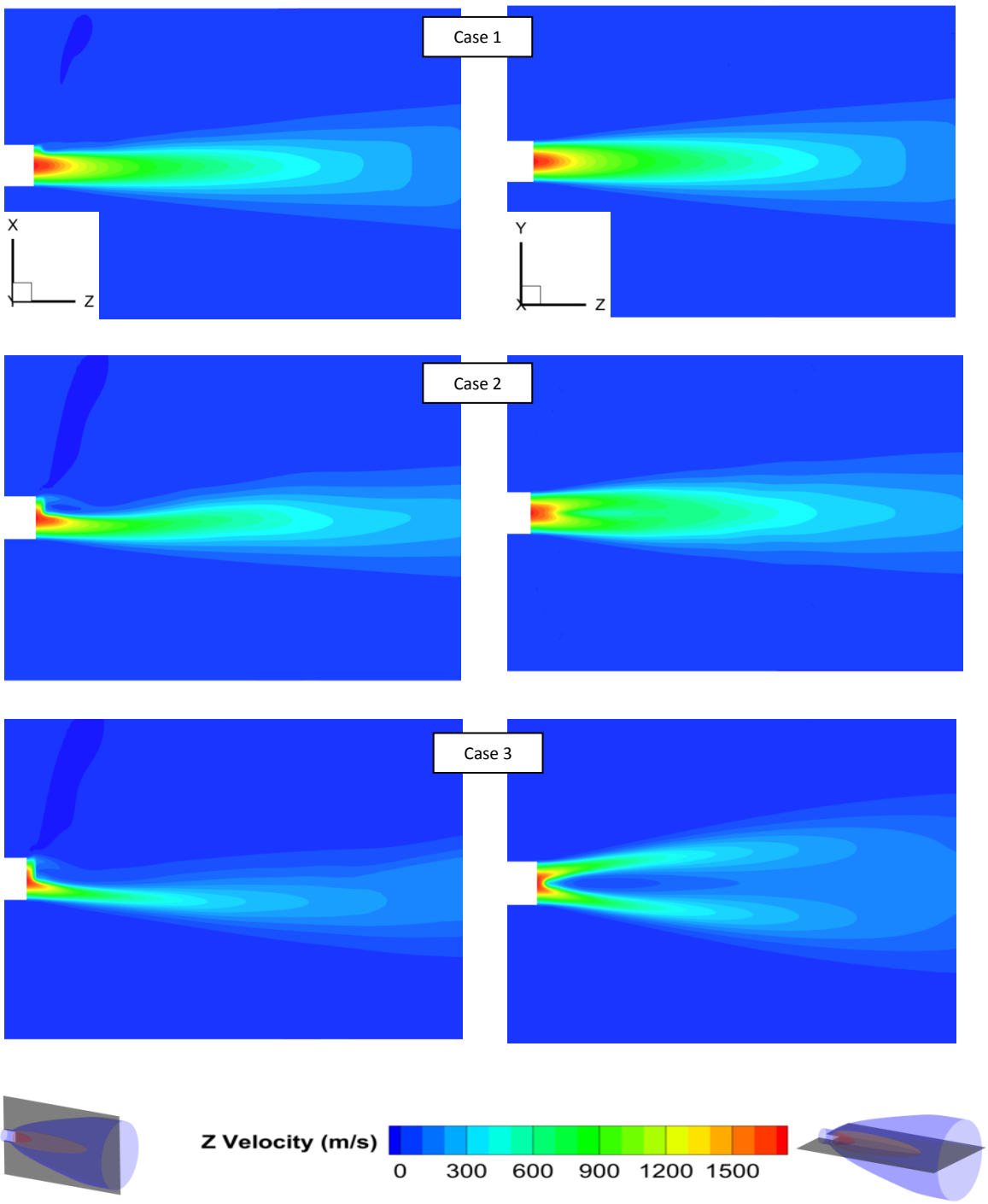

Figure 3.4 Effect of suspension injection on axial velocity profile, left hand side is Y-Z plane (injection is in this plane), and right hand side is X-Z plane.

In addition, the same investigation is performed on the temperature profile of the plasma plume. Figure 3.5 illustrates the gas phase temperature contours obtained by KHRT and RSM models when the suspension mass flow rates are 0.23 g/s (case 1), 0.45 g/s (case 2) and 0.68 g/s (case 3). The temperature reduction in the plasma plume because of the suspension penetration is shown in this figure. The Y-Z plane in figure 3.17 completely clarifies that the suspension in case 1 could not penetrate to the plume; and in case 3 it completely went through the plume and did not allow the plume to rearrange the circular shape [11].

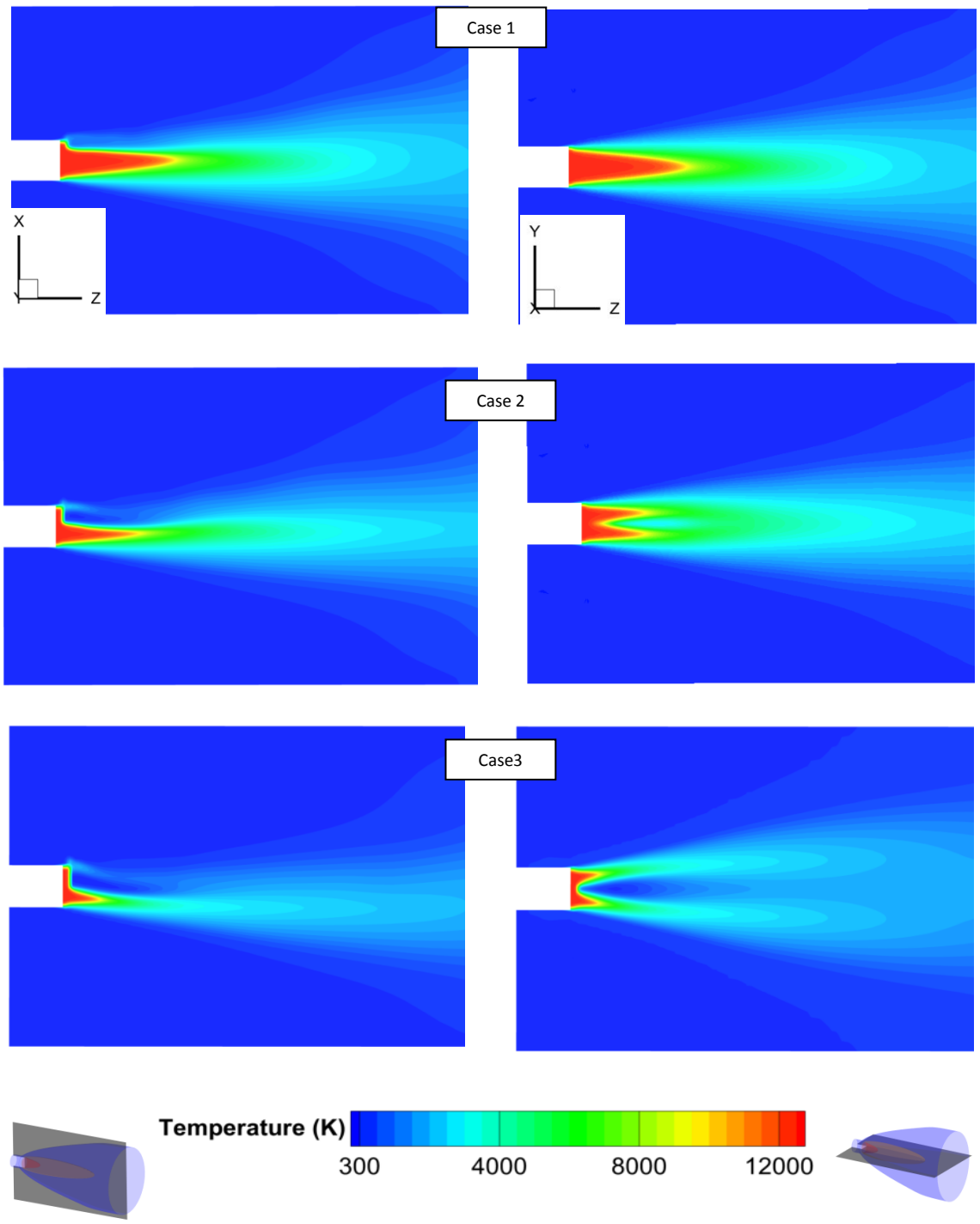

Figure 3. 5 Effect of suspension injection on temperature profile, right hand side is X-Z plane and left hand side is Y-Z plane

In addition, the temperature profile in the X-Y plane (i.e. across the plasma jet) is studied. In Figure 3.6 the temperature contours of cases 1, 2 and 3 are shown, respectively. These graphs show the penetration of suspension in a plane normal to the plasma flow (X-Y plane). Insufficient penetration in case 1 is clear, and in addition, excessive penetration in case 3 is observed again. In cases 1 and 2 the plume can rearrange the circular shape; but in case, 3 due to high velocity and mass flow rate of suspension, the plasma plume cannot come back to the circular shape [11].

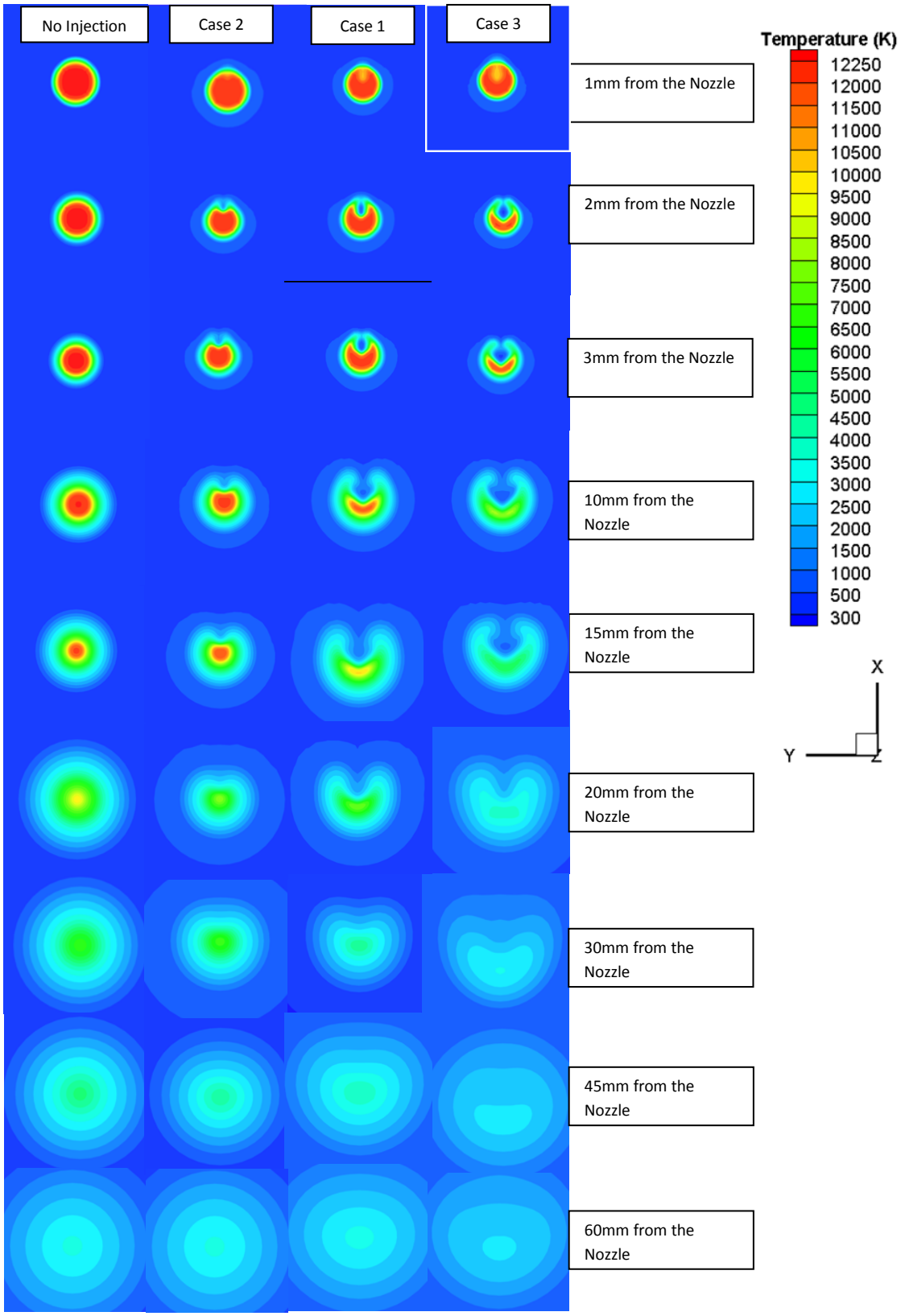

Figure 3.6 X-Y plane temperature profile of each case in different distance

3.3. Discrete phase

As mentioned above, there are seven cases studied in this work. The first case is the optimum case, on which experimental results are based. In addition, for validation of our results, representative experiments are conducted for cases two and three. In this part, for the first step, results of two breakup models are compared. In Figure 3.7 two secondary breakup models (TAB and KHRT) are compared [10] and particle trajectories and temperatures and velocities for cases 1, 2, 6 and 7 are illustrated [10, 11]. The TAB method results in larger droplets; in other words, it results in fewer breakups. It should be mentioned, in KHRT breakup some small droplet can form that in reality they cannot carry any particles (droplet size is less than particle size) and they will evaporate very fast. In this modeling, each droplet is like parcel that has nickel particle (15% of mass). These parcels or droplets after evaporation can produce very small size particles. These particles are filtered because presence of them are not realistic (in reality those small parcel or droplet could not carry any particle). Moreover, filtering of them doesn't affect our modeling because they are few in numbers.

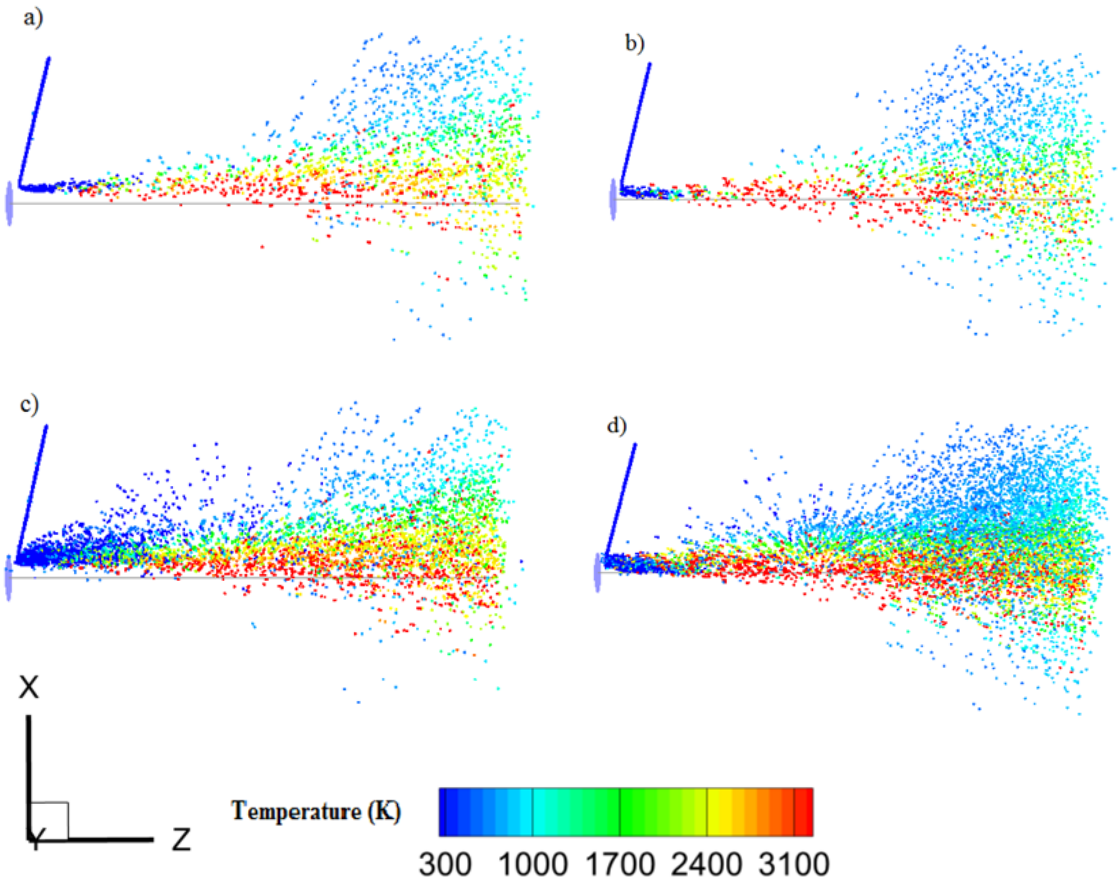

Figure 3. 7 Comparison of TAB and KHRT breakup models using two different mass flow rates. a) case 6 (TAB, mass flow 0.23gr/s), b) case 7(TAB, mass flow 0.45gr/s, c) case 2 (KHRT. Mass flow 0.23gr/s, d) case 1 (KHRT, mass flow rate 0.45gr/s) [10]

Moreover, it is clear that the suspension penetration in cases 1 and 7 is more than that in cases 2 and 6, due to the increase in mass flow rate and velocity of suspension. As can be seen from this figure, the KHRT model produces more droplets, as expected. KHRT is more suitable for catastrophic breakup modeling, and the breakup of the suspension in the plasma plume is categorized as a catastrophic breakup [4].

Figure 3.7 shows that for case 1, the penetration of suspension into the plasma plume is not enough, which results in fewer breakups and longer time for the evaporation of the droplet. Therefore, fewer nickel particles can reach to the melting point temperature. To find the condition for optimum suspension penetration, numerical results of cases 1, 2 and 3 are compared in Figures 3.8, 3.9, and 3.10, where the particles temperature distributions are compared at a stand-off distance of 8cm in the X-Y plane. Studying behavior of particles in this stand-off distance doesn't mean that we can put substrate here. The optimum stand-off distance for substrate will be investigate further.

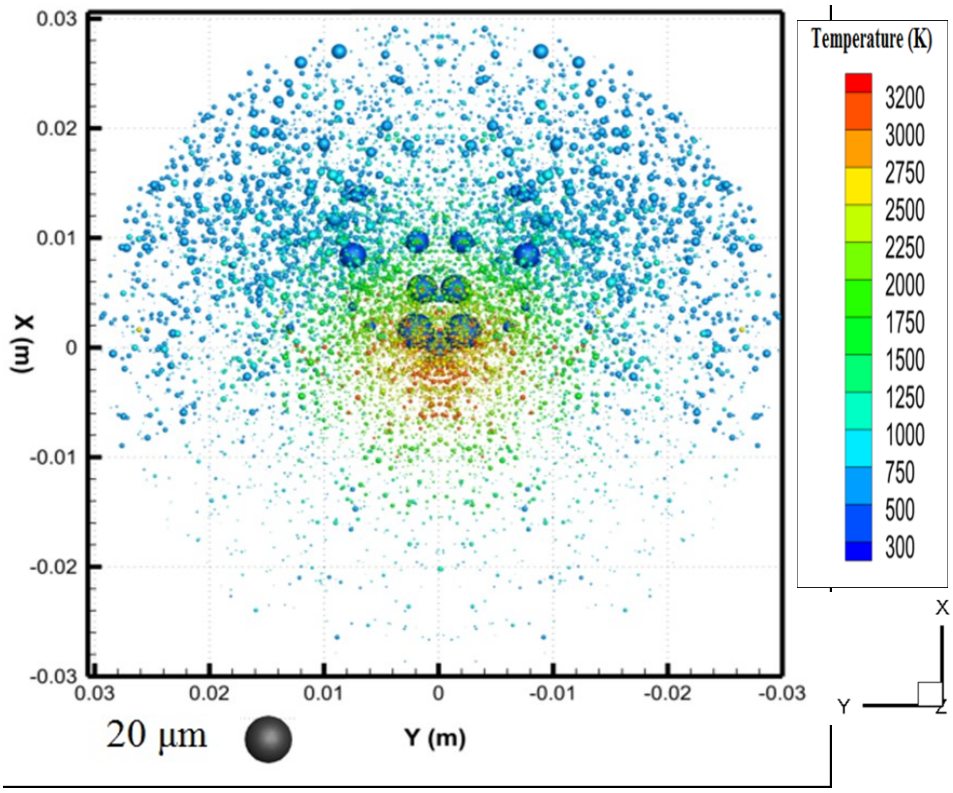

Figure 3. 8 Temperature of particles in X-Y plane, mass flow of suspension 0.68 gr/s, V =38.6/s

As is clear in case 1 (Figure 3.10), the penetration of suspension is poor, as most of the suspension cannot penetrate to the plume and most of it will be wasted. In all figures the magnification of 200 times is used to clarify the position of suspension droplets and particles. Large droplets in case 1 (Figure 3.10??) are due to the lack of penetration of suspension in the plasma plume.

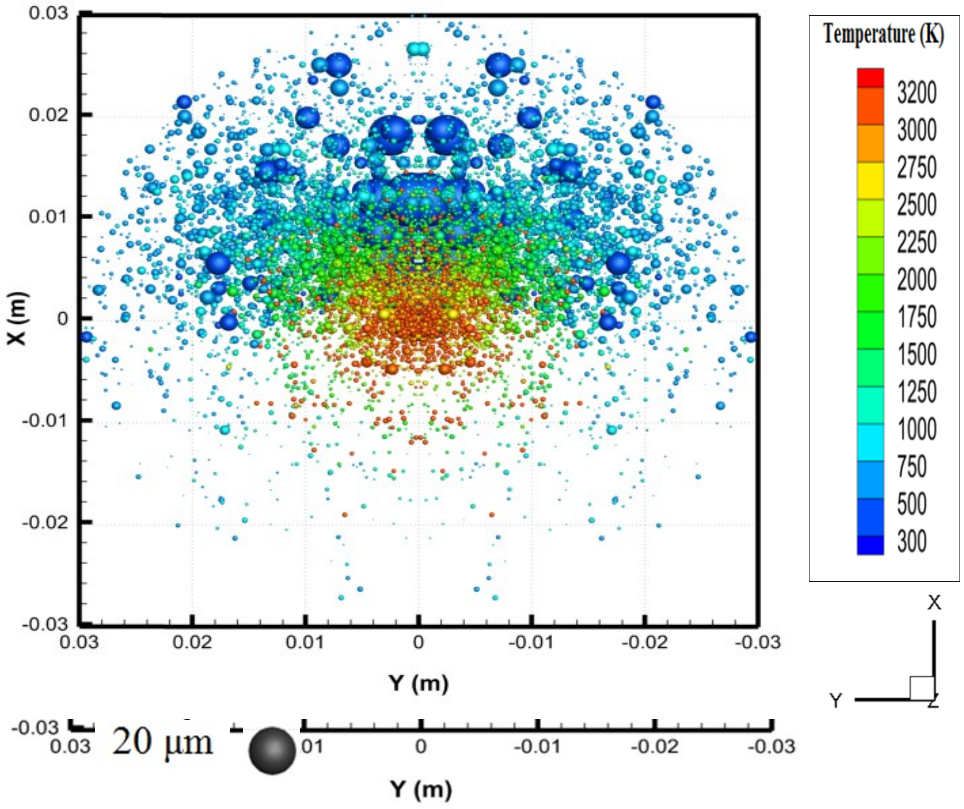

Figure 3.9 Temperature of particles in X-Y plane, mass flow of suspension 0. 32 gr/s, V =25.7 m/s

As mentioned above, less penetration will result in fewer breakups and consequently results in large droplets and incomplete evaporation of base liquid. It is clear that incomplete evaporation of base liquid results in poor coating. This

issue is shown in Figure 3.10; very large droplets are formed above the centerline due to lack of penetration, these large droplet will not evaporate resulting in unmelted nickel particles which cannot be deposited.

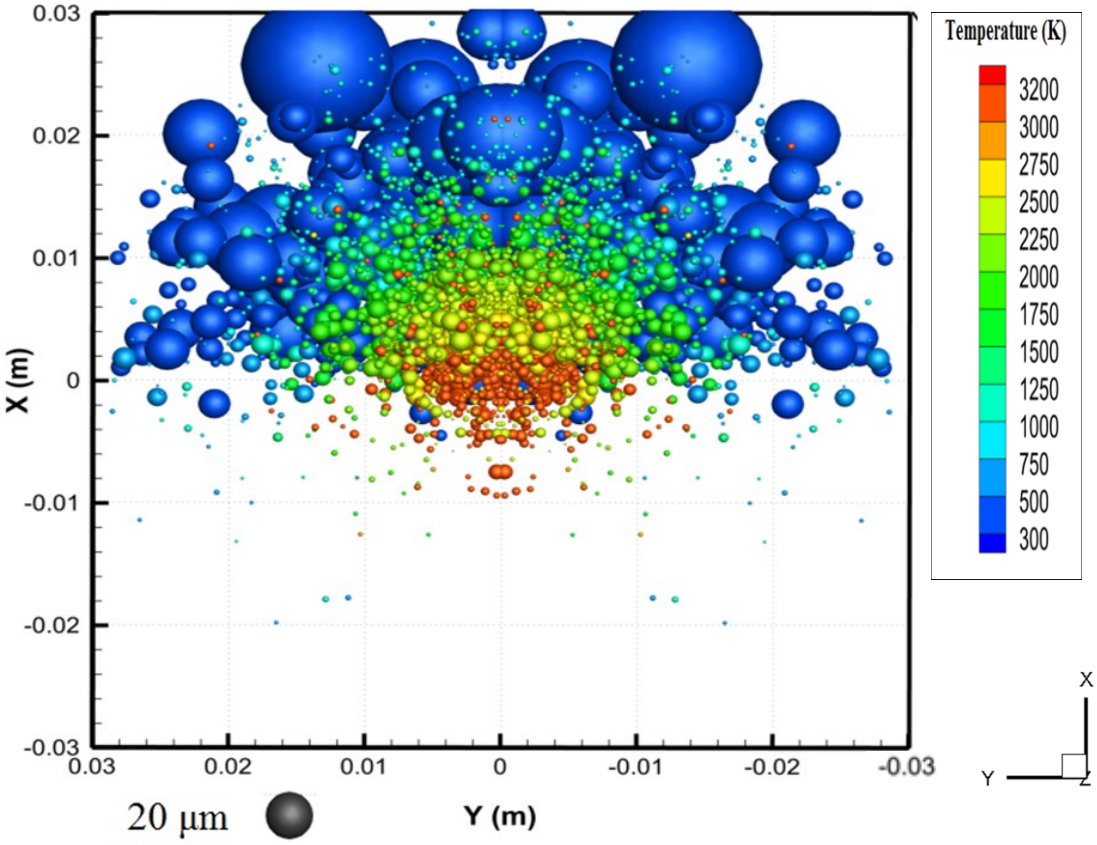

Figure 3.10 Temperature of particles in X-Y plane, mass flow of suspension 0. 23 gr/s, V = 12.9 m/s

It should be mentioned that in this modeling there is no substrate, and the optimum position are found based on temperature and velocity distributions of particles at various stand-off distances. Figures 3.11 and 3.12 illustrate velocity and temperature of particles at different distance from the nozzle. It should be mentioned that in these Figures up to 60mm standoff distance from the nozzle

are shown and the rest of the results are in Appendix 1. For example, in Figure 3.11 it is clear that for stand-off distances larger than 5 cm the particle velocity is reduced, therefore it is not recommended to place the substrates at stand-off distances larger than 5 cm. Moreover as shown in Figure 3.12, for stand-off distances less than 3 cm, the temperature of particles is very low, and it is clear in this figure that at 2 cm from the nozzle the majority of base liquid is not evaporated yet. When temperatures of particles are too low (less than the melting point), they will not stick to the substrate. Therefore, based on the results shown in Figures 3.11 and 3.12 one can determine the window of operation for substrate stand-off distance; it should be placed at a distance of larger than 3 cm and smaller than 5 cm. Similar investigations of velocity and temperature of particles are also done for cases 1 and 3 and the results are shown in Appendix 2.

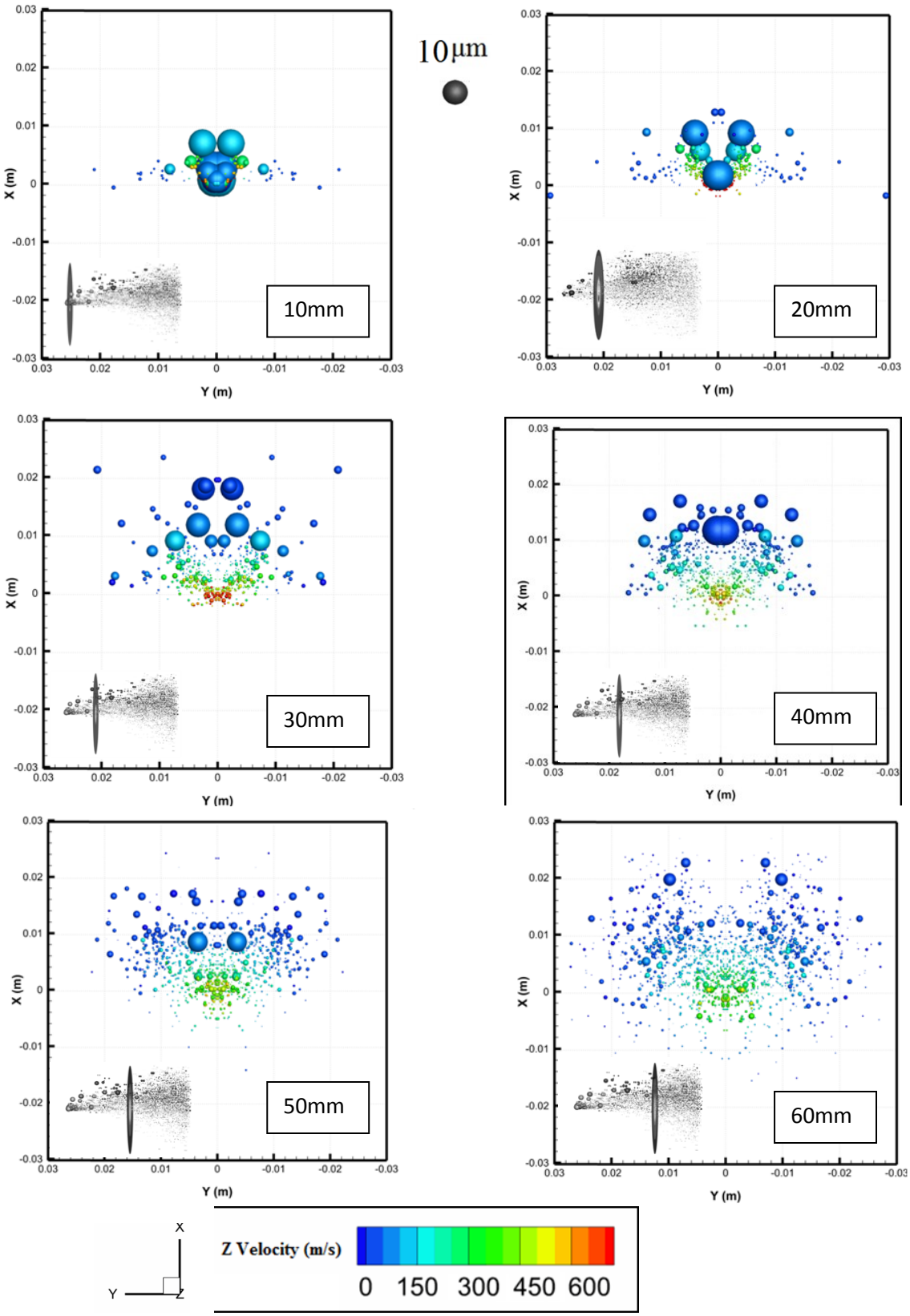

Figure 3.11 Particle distributions at different stand-off distances, colors show particle axial velocity (case 2, 0.45 g/s, 25.7 m/s)

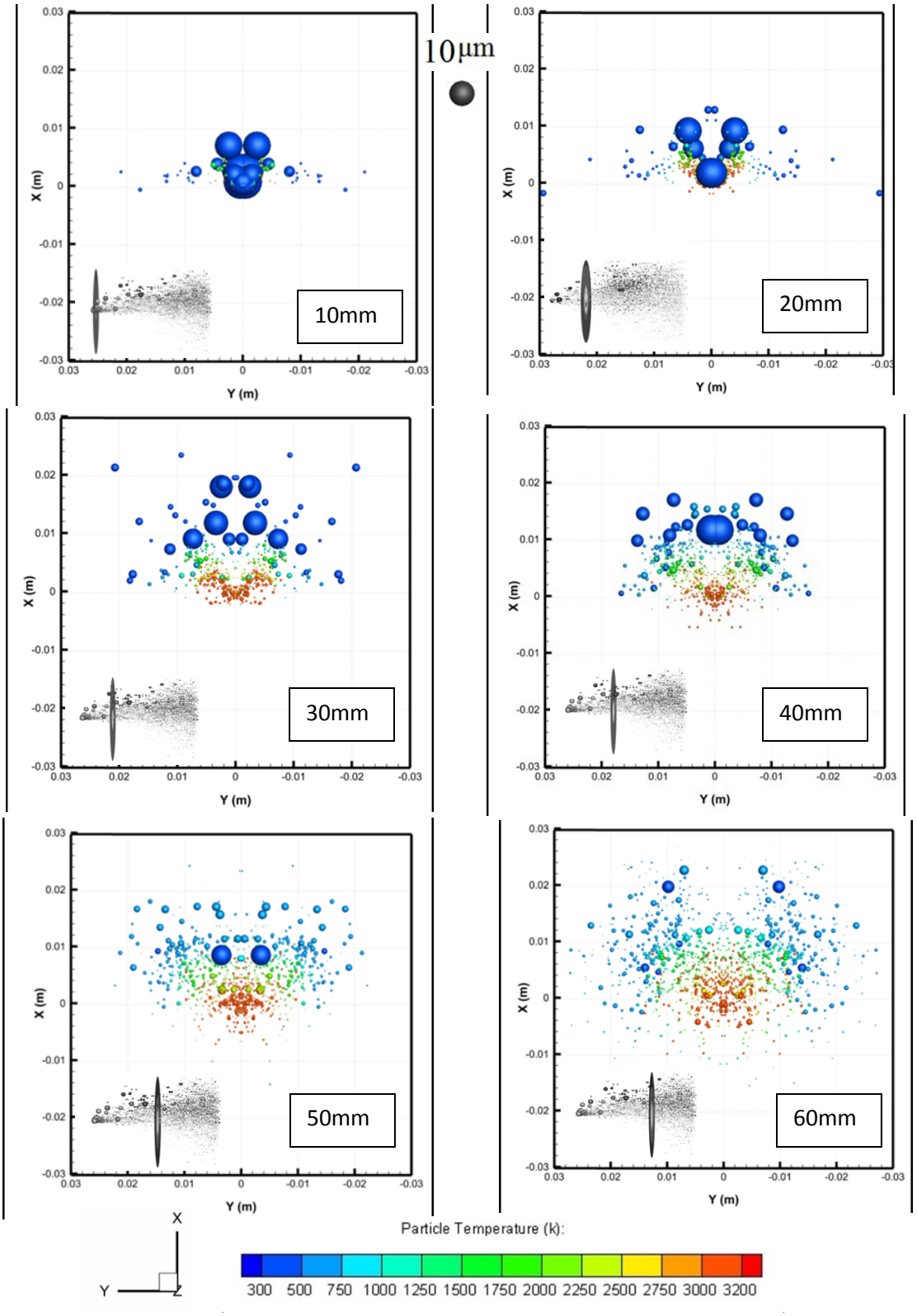

Figure 3.12 Particle distributions at different stand-off distances, colors show temperature of particles, (case 2, 0.45 g/s, 25.7 m/s)

For more clarification on the recommended place for substrate it is better to show the results in X-Z plane. Figure 3.13 to 3.15 show the temperature and velocity of cases 1, 2 and 3 in the X-Z plane.

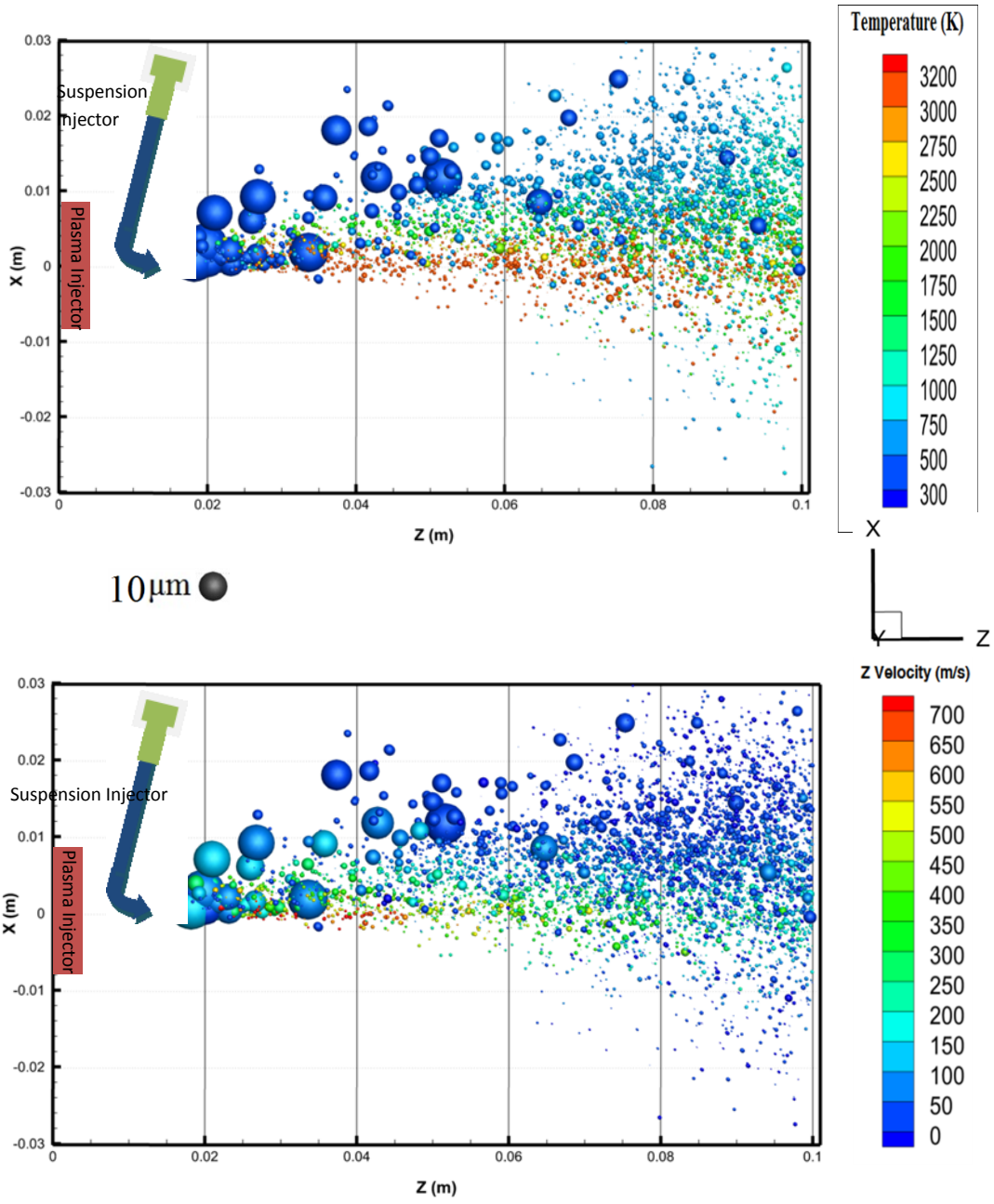

Figure 3.13 Particle trajectory for Case 1 in X-Z plane, magnification of 200 times, case 2

In Figure 3.13 it is clear that particles flying near the centerline reach higher temperature in comparison to other particles. Moreover, after 5cm the velocity is reduced significantly.

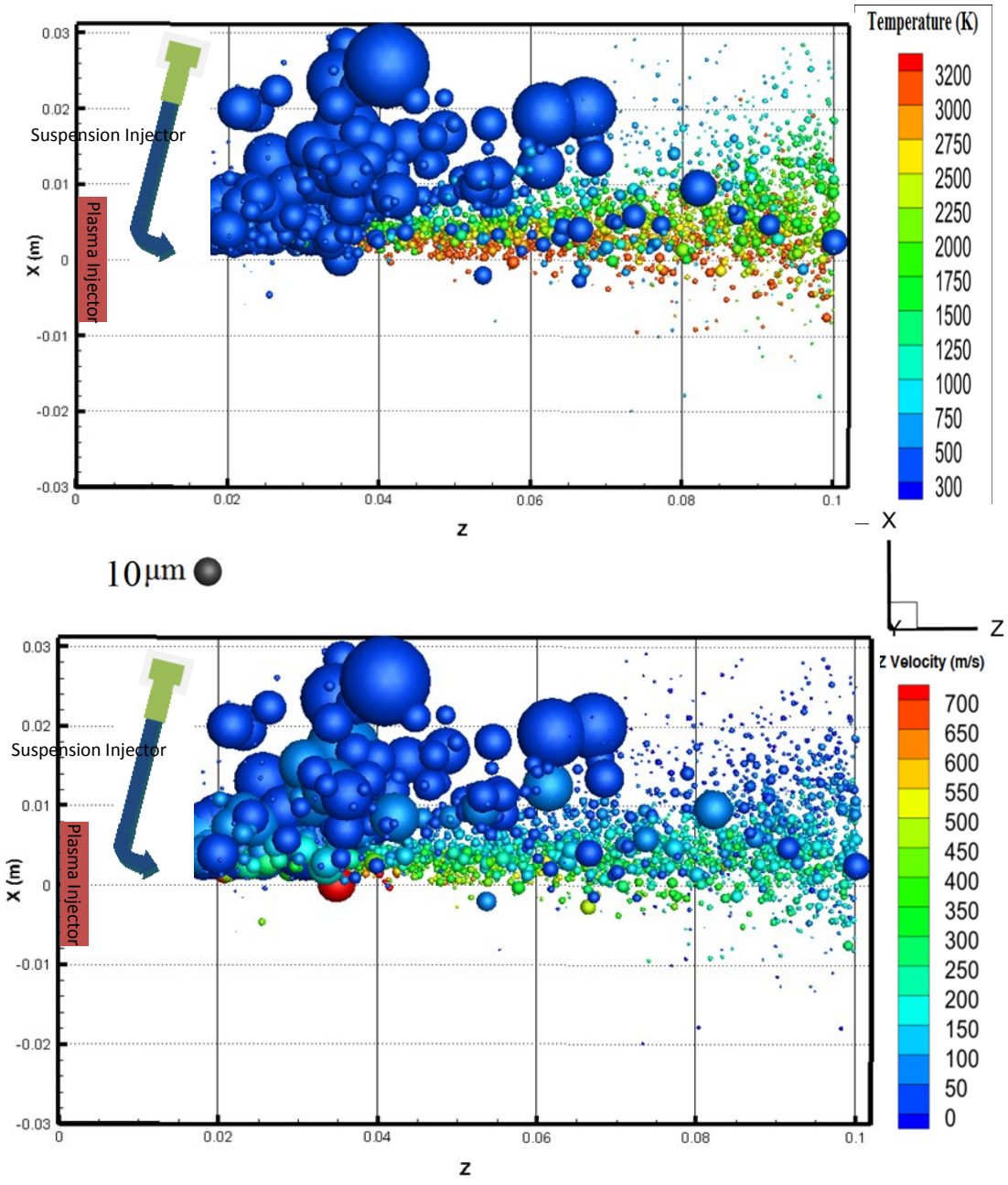

Figure 3. 14 Particle trajectory for Case 2 in X-Z plane, magnification of 200 times, case 1

In Figure 3.14 the lack of penetration of suspension results in fewer breakups. Large droplets, around $100\mu m$, in this figure represent wasting of feedstock because when the breakup is not complete, the droplet evaporation will not be complete which means that there are not enough molten particles to form well-adhered coatings.

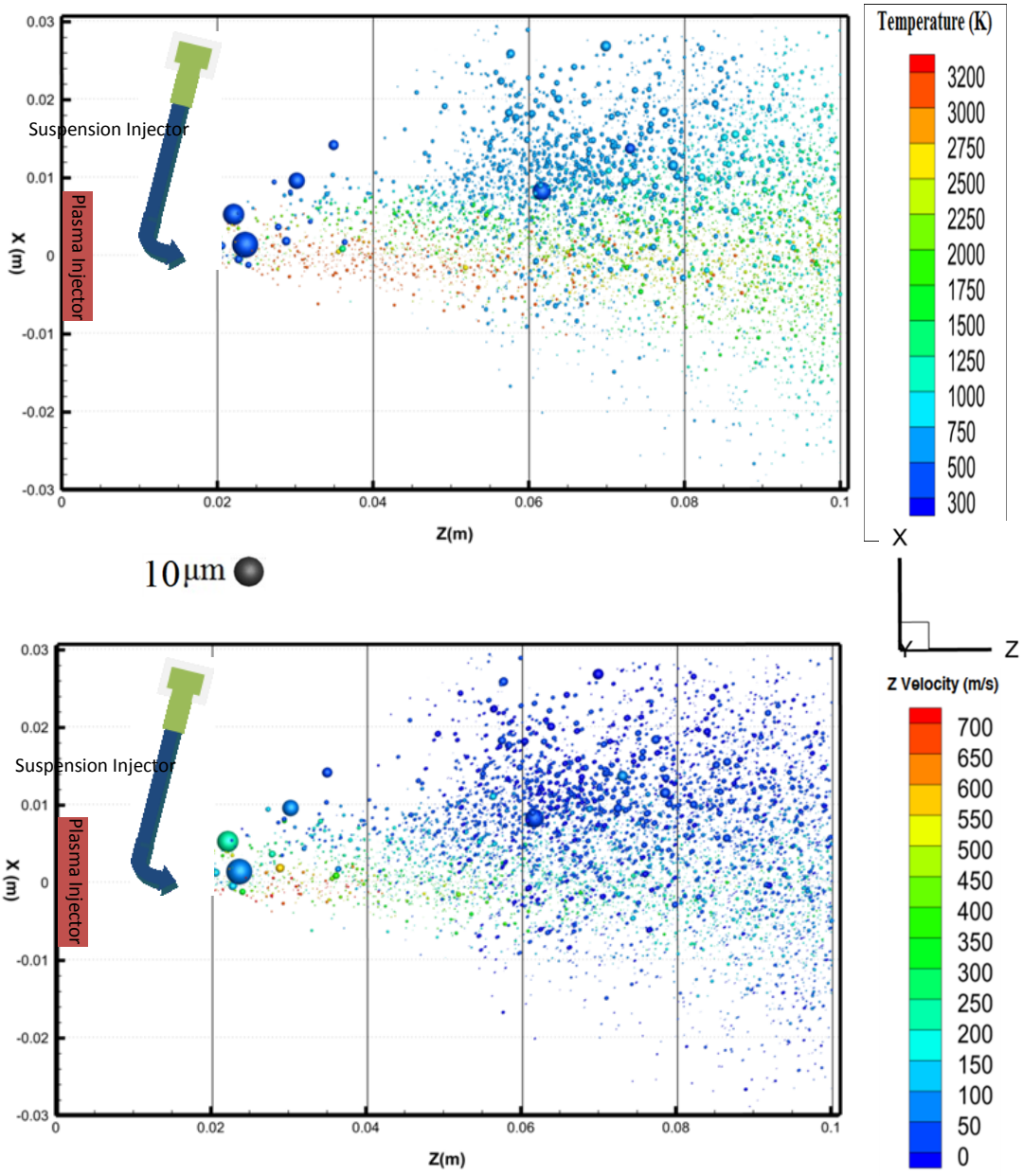

Figure 3. 15 Particle trajectory for Case 3 in X-Z plane, magnification of 200 times, case 3

In figure 3.15 (case 3) it is clear that the amount of particles that reach temperatures above 2500 K is less than that in case 2. It should be mentioned that the suspension penetration in case 3 is greater than that in case 2 due to the greater momentum that the suspension has in this case. Although greater

penetration results in higher temperature, the plasma plume has limited capacity when the amount of suspension is very high, as the plume cannot melt all particles. Nickel particles that move near the centerline can reach higher temperature.

In addition, in order to compare the penetration of suspension in cases 1, 2 and 3 one can show the particles and center plane together in one picture for each case. Figure 3.16 can be used to compare the penetration of these three cases. As it is clear in this figure, in case 1 due to the insufficient penetration, the majority of suspension cannot reach the center plane. Moreover, case number 3 can penetrate to the plume very well, however as it mentioned the problem for this case is limited source of heat, on the other word plasma plume couldn't heat up this mass flow rate.

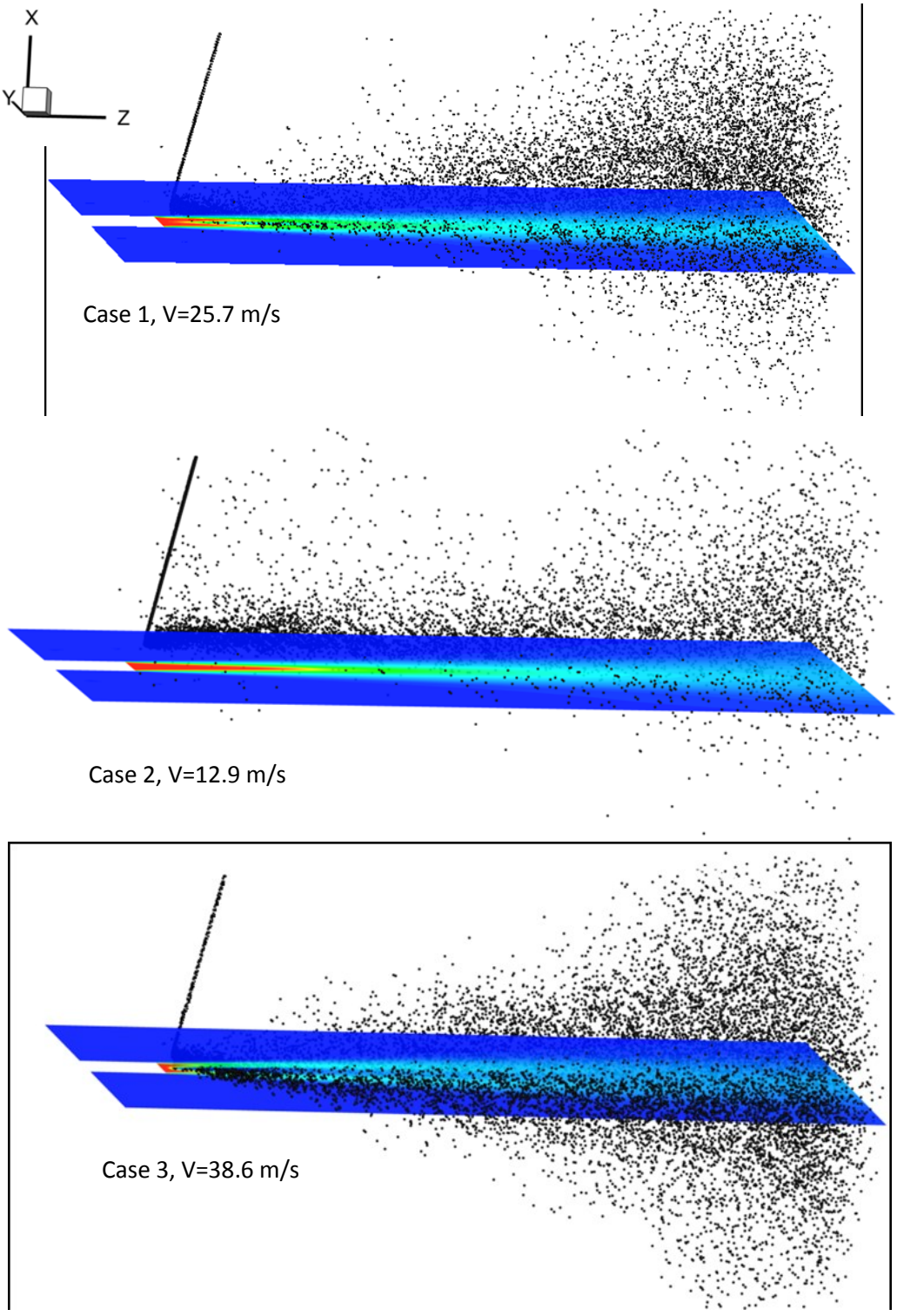

Figure 3.16 Particle trajectories for case numbers 1, 2 and 3

Figures 3.17-3.19 show the cumulative particle size distribution, particle temperature and particle velocity as a function of particle counts (%) at 4, 5, 6 cm from the nozzle exit for case 2. The characteristics of those particles that are inside a 2x2 cm^2 window (the size is similar to the substrate size in the experimental part of the study [6] at the nozzle centerline (-1<X<1cm and -1<Y<1cm in Figures 3.17 to 3.19) are collected and analyzed to draw the curves in Figures 3.17-3.19. As mentioned above, at 3 cm from the nozzle exit, there are many particles with very high velocity and temperature close to the centerline. However, many particles/droplets with very low velocity and temperature exist away from the centerline. Therefore, the results at 3 cm from the nozzle exit are not plotted in Figures 3.17-19.

Figures 3.17 and 3.18 show that the ensemble distribution of particle size and temperature do not significantly vary for various stand-off distances. In contrary, as shown in Figure 3.19, at 4cm from the nozzle exit, many particles reach the velocity higher than 400 m/s. As the distance from the nozzle exit increases, the number of particles with high velocity (the velocity higher than 400 m/s) decreases. On the other hand, with increasing distance from the nozzle exit, the number of particles with low velocity (the velocity less than 400 m/s) increases. It should be noted that the kinetic energy of the particles is one of the most important parameter to achieve a strong bond between the material of the

coating and the substrate. As mentioned, with increasing the stand-off distance from 4 to 6 cm, the number of small particles with low velocity increases. Thus, the porosity is expected to increase. The small particles with low relative velocities strongly follow the gas phase streamlines. In other words, when the plasma jet is impinging on a substrate, these particles slow down and get diverted by the flow in the stagnation region. It has been experimentally indicated that the porosity increases as the distance from the nozzle exit grows [6].

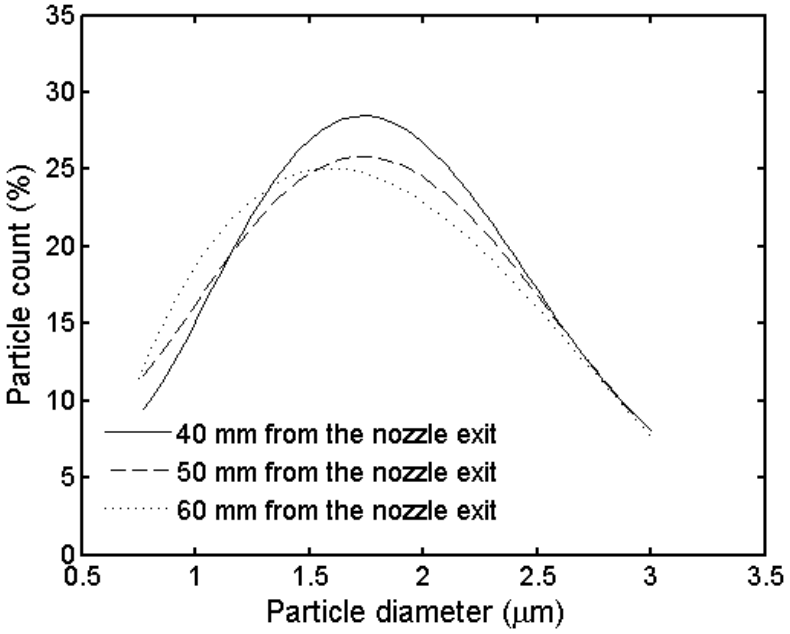

Figure 3.17 Particle-size distributions as a function of particle count at different distances from the nozzle exit inside a 2 x 2 cm^2 window at the nozzle centerline. The suspension injection velocity is 25.7 m/s [11]

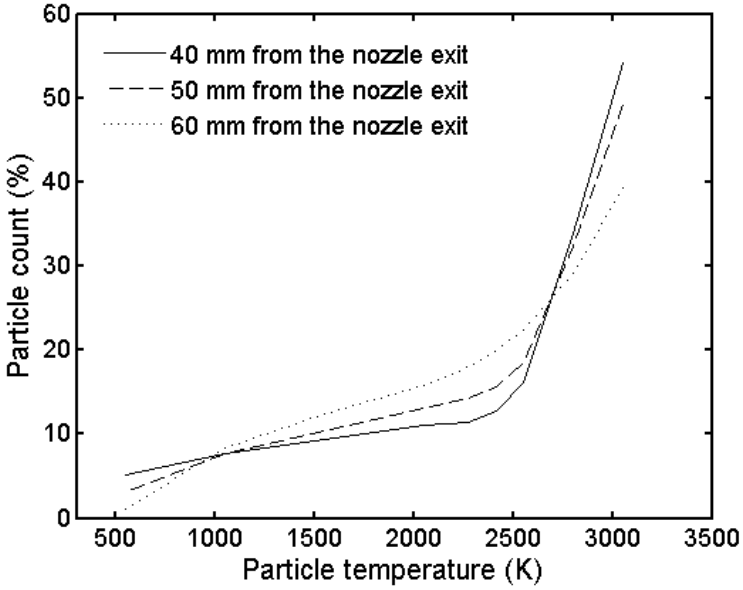

Figure 3.18 Particle temperature profiles as a function of particle count at different distances from the nozzle exit inside a 2 x 2 cm^2 window at the nozzle centerline. The suspension injection velocity is 25.7 m/s [11]

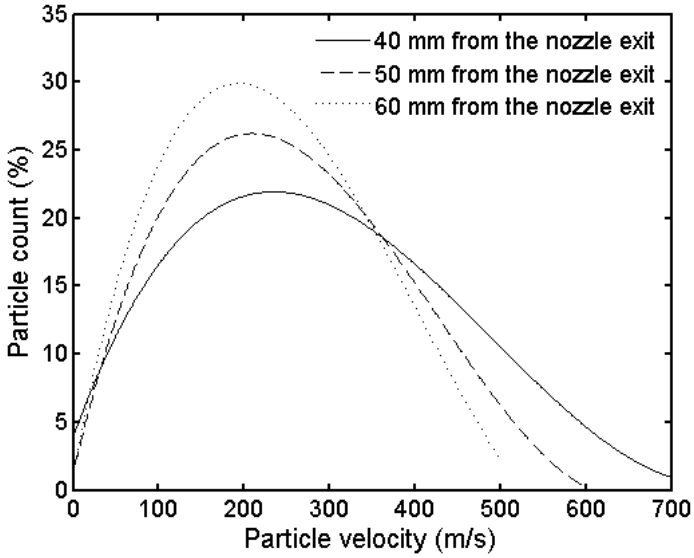

Figure 3.19 Particle velocity profiles as a function of particle count at different distances from the nozzle exit inside a 2 x 2 cm^2 window at the nozzle centerline. The suspension injection velocity is 25.7 m/s [11]

The last part of numerical results is the investigation on changing the angle and position of suspension injection nozzle. As it is mentioned in table 3.1, in case 4 the injection angel is changed to 0° and in case 5 the suspension injector is shifted 1cm further away from the plasma gun. Figure 3.20 shows the trajectory of particles for cases 4 and 5 and compares them with those of case 2. As it is clear in Figure 3.20, specially in left hand side of the figure, by changing the injection angel to zero degree or shifting the injector 1cm further away from the plasma nozzle the penetration of suspension and the resultant particle trajectories are worse.

When the injector is shifted 1cm further away from the plasma gun due to the reduction in speed of plasma the penetration should be improved. However, more distance from the plasma gun results in lower gas temperature that results in higher density. It should be mentioned that greater gas density results from two factors: the first one is due to the decrease in temperature of plasma plume and the second one is due to the fact that the ambient air is mixed more with the plasma flow. Furthermore, as the suspension breakup starts sooner, the penetration of small droplets are less possible which will further contribute to the lack of suspension penetration to the plasma plume.

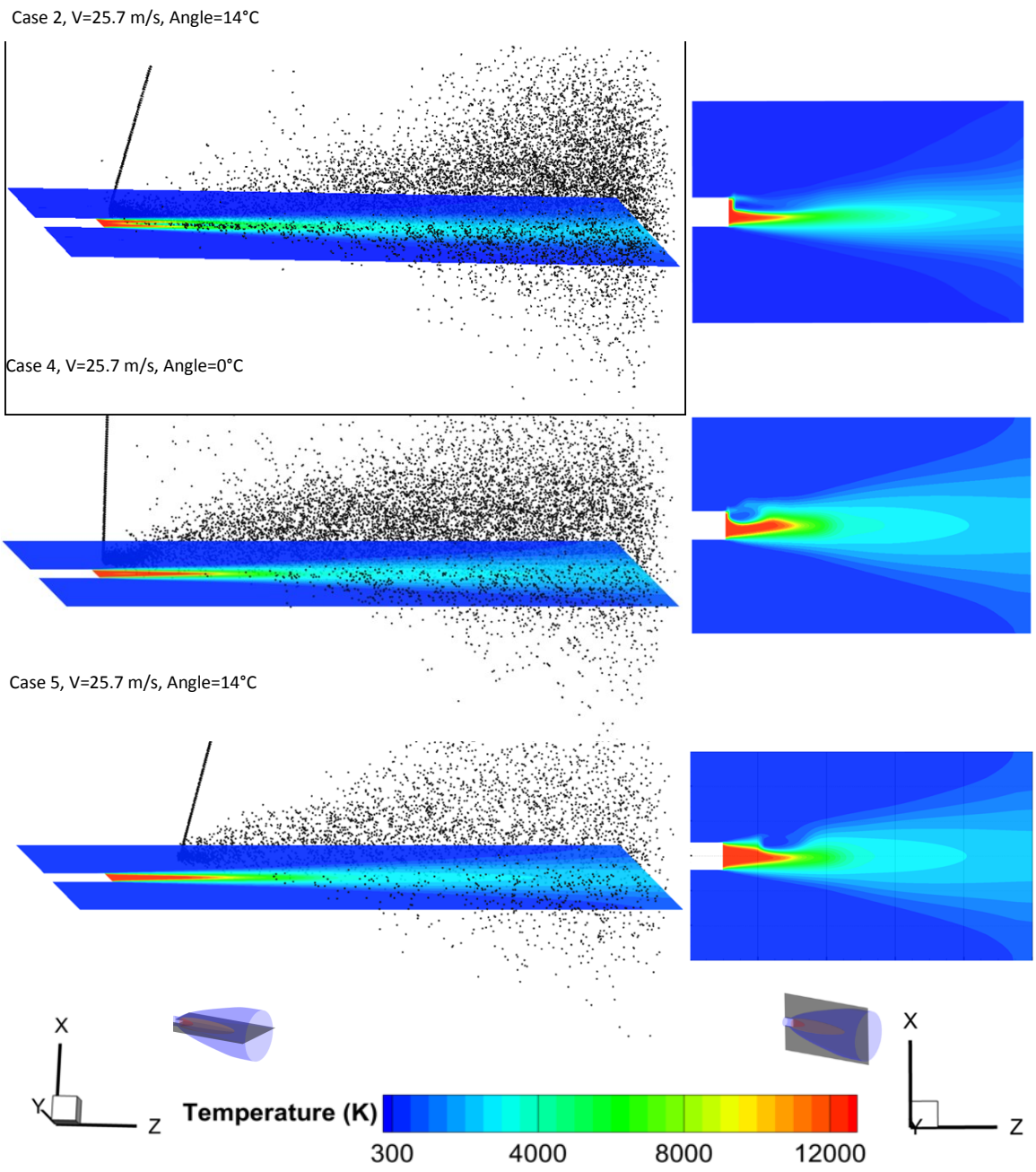

Figure 3. 20 Left, particle trajectories for cases 2, 4 and 5 with presence of center plane that shows temperature profile, and Right, temperature profile of symmetry plane

3.4. Experimental validations

Validating experiments have been performed using high speed imaging, Fotron camera, FASTCAM 1.1 model, with 10,000 frames per second. Argon flow rate was 45 slpm (standard liter per minute), voltage was 60 V, and current was 470 A. Pure water was used for both simulation and experiment. The water mass flow rates were 0.20 g/s and 0.5 g/s. The water tank pressures for the experiment were 25and 75 psi which were equivalent to the mass flow rates around 0.20 g/s and 0.5 g/s. Figure 3.21 shows the schematic of suspension tank. Compressed air pushes suspension into the delivery pipe. This kind of tank can be used for suspension, solution or pure liquid. In the current work we used it for pure water.

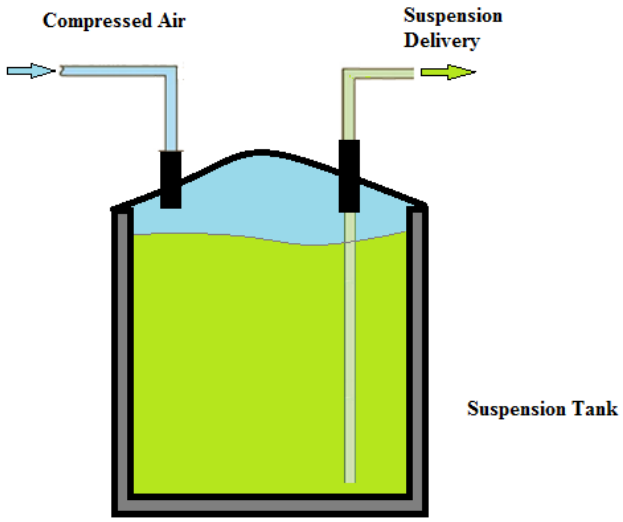

Figure 3.21 Schematic of the pressure tank

Figure 3.22 shows the experimental results with and without using an optical band-pass filter. A band-pass filter transmits light within a defined spectral band (532 nm). Figure 8-a shows the image obtained without using an optical band-pass filter and with no water injection. In Figure 8-b and c the filter (532BP10) is used and the water mass flow rates are 0.25, and 0.5 g/s, respectively.

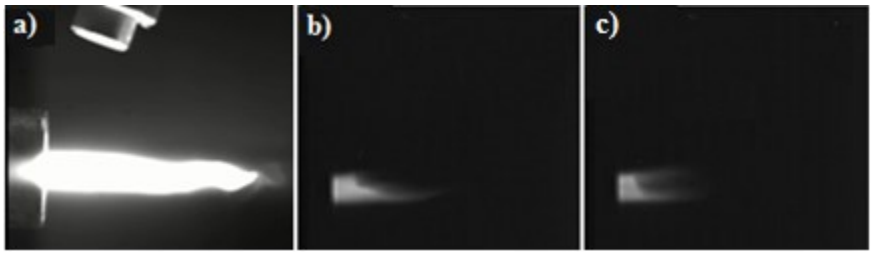

Figure 3.22 Visualization of plasma flow with liquid injection (a) without using the optical filter, (b) injection velocity of 11 m/s using the optical filter, (c) injection velocity of 28 m/s using the optical filter

Figure 3.23 shows the comparison between time-averaged experimental data and numerical results in terms of water penetration depth. As can be seen, the trend of simulation results are in good agreement with the experiments. The lower penetration depth predicted by the numerical simulations compared to the experimental results can be attributed to the fact that in this work the primary atomization is not directly modeled. To model the primary atomization,

interface-tracking methods such as volume of fluid (VOF) or level set can be used. Although they are effective in terms of modeling primary atomization, they need very fine mesh and are extremely time consuming.

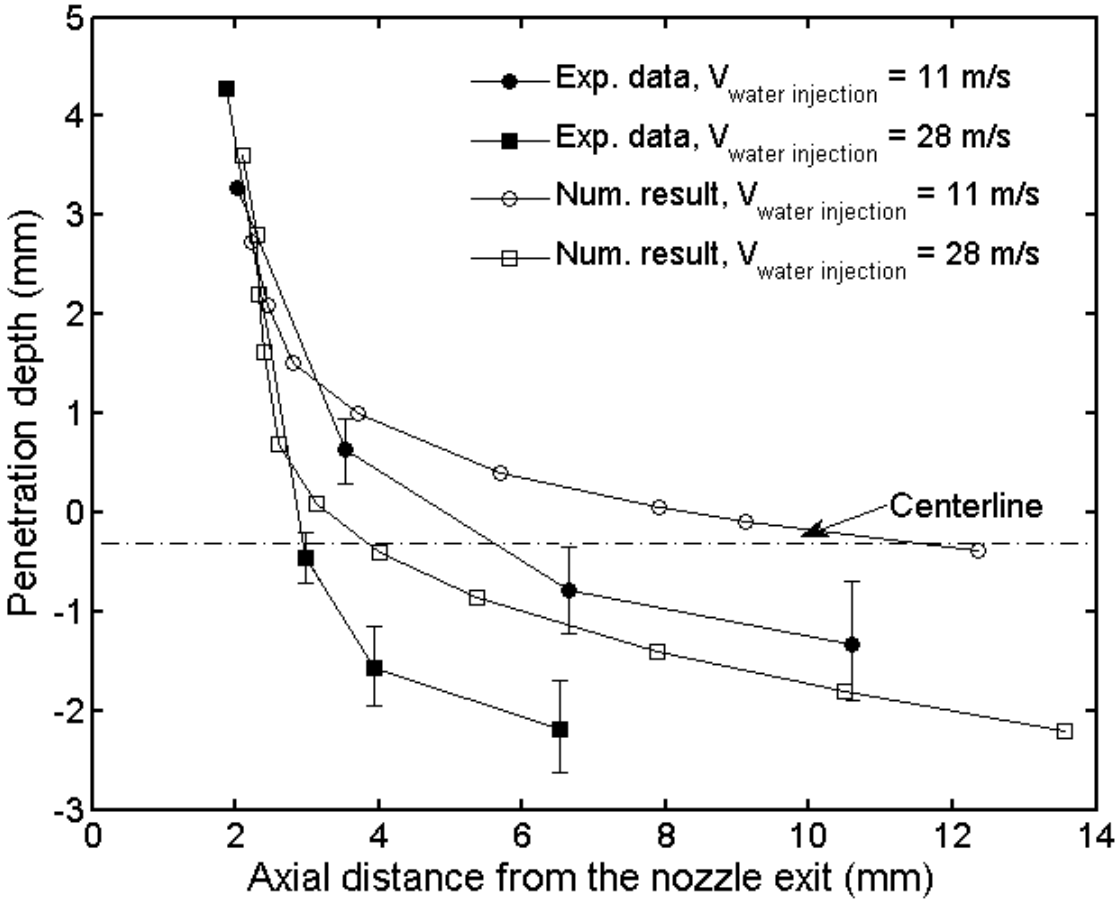

Figure 3.23 The comparison between the experimental and numerical results for the depth of water penetration in the plasma plume

3.5. Grid Dependency Test

A grid dependency test is performed on the free jet modeling without suspension injection. A fine mesh with 8 folds more nodes than the one that is used in this study is utilized. The plasma plume temperature along the centerline of the domain for the fine and coarse grid are presented in Figure 3.24. The difference between the two results for capturing the plasma temperature profile is negligible. It should be mentioned that computation time with the current mesh is almost ten times faster than the one with the finer mesh.

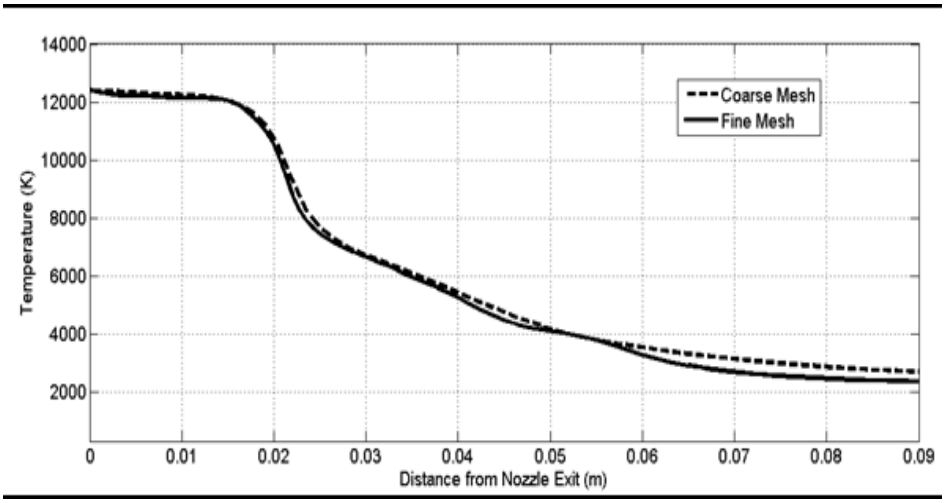

Figure 3.24 Plasma temperature along the centerline for coarse and fine mesh

4. CONCLUSIONS AND FUTURE WORKS

In this chapter

Conclusion of this study will be covered. In addition, future work and some preliminary results of that will be discussed.

This work has two main steps: the first is modeling of the plasma plume without any injection, and the second does so with injection of suspension. To model only the plasma flow a 2D-Axisymmetric domain is capable of giving acceptable results. However the main goal of this work is not only modeling of plasma flow, but also studying the behaviour of a suspension that is injected radially in the plasma flow. To model this kind of flow, a 3D modeling is required. To reduce time and cost of modeling, half of the domain is modeled. In the first part, the main goal was achieving the correct temperature profile in the high-temperature zone. To fulfill this goal, two turbulence methods were compared (k-ε and RSM). Although RSM is time-consuming and more difficult to achieve converging, it is proven that the RSM result is more accurate, especially in the high-temperature zone of the plume. In other words, the k-ε model cannot predict the high-temperature zone and it underestimates the length of this zone. When suspension is injected into a plume that predicted by k-ε model, temperature of nickel particles after evaporation of the base liquid will be very low and a majority of particles cannot reach the melting point. To validate these results, they were compared to other numerical and experimental results.

After validating the plasma flow results, the solver is coupled with the discrete phase to model the suspension and particle flows. It should be

mentioned that two-way coupling is utilized, which means that the effect of the gas phase on particles and the effect of the particles on the gas phase both are considered. In APS modeling where only solid particles are injected, since the surface tension of molten particles is very high, no breakup will happen. However, in the SPS process, breakup plays a significant role. In other words, without breakup of suspension droplets no coating will form. Breakup of droplets is mainly governed by the droplet Weber number. Based on high and low Weber numbers, two breakup models were compared i.e. TAB and KHRT. It was shown that the results using KHRT are more realistic since this model is designed for catastrophic breakups with high Weber numbers typical of those in SPS process .

Finally a parametric study was performed to shed more light on the effect of various parameters on the performance of a SPS system. Particle temperature, velocity, and trajectory have been studied for each case to find the optimum position for the substrate. In addition, optimum flow rate for suspension was investigated. It can be recommended that if the distance between the nozzle exit and the substrate is around 4 cm, most likely coatings with higher quality can be produced, because the particles' temperatures and velocities are the highest at this distance. The effects of the suspension mass flow rates on the penetration depth and particles' temperature and velocity have also been simulated and

discussed. Furthermore, some validating experiments were performed to support the numerical results.

Future work can be classified in following several steps.

- As a first step in future work, substrate should be added to the domain, and the effect of substrate on the main gas flow and deposition of particles on substrate should be investigated. Figure 4.1 shows symmetry plane mesh. The black area in this figure represent the substrate. It is clear that meshing method should be changed and cells near substrate should be fine like Figure 4.1. Figure 4.2 shows the effect of substrate on the main flow. Small vortexes are due to presence of substrate. Modeling injection is more challenging in the presence of these vortexes. By changing the stand-off distance of substrate, position and magnitude of these vortexes are changed.

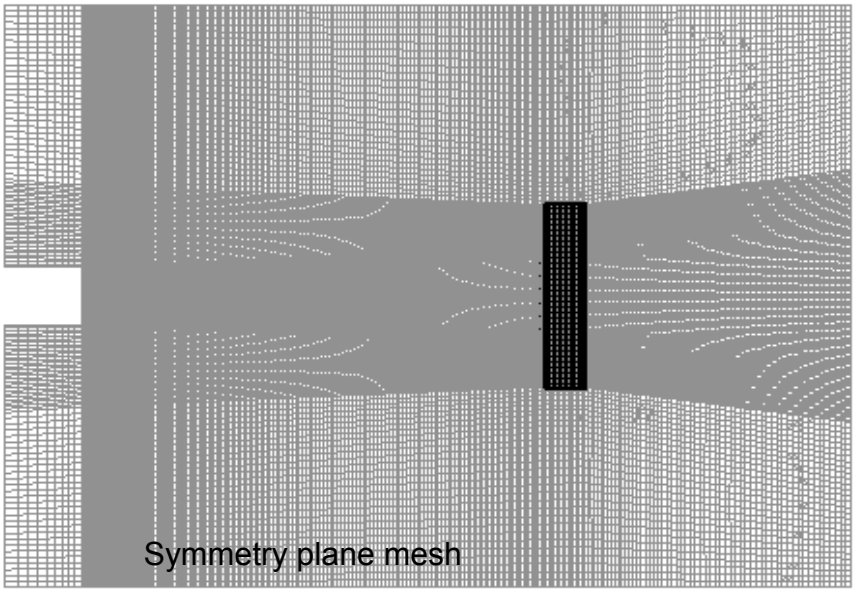

Figure 4.1 Mesh of plane of symmetry with a flat substrate

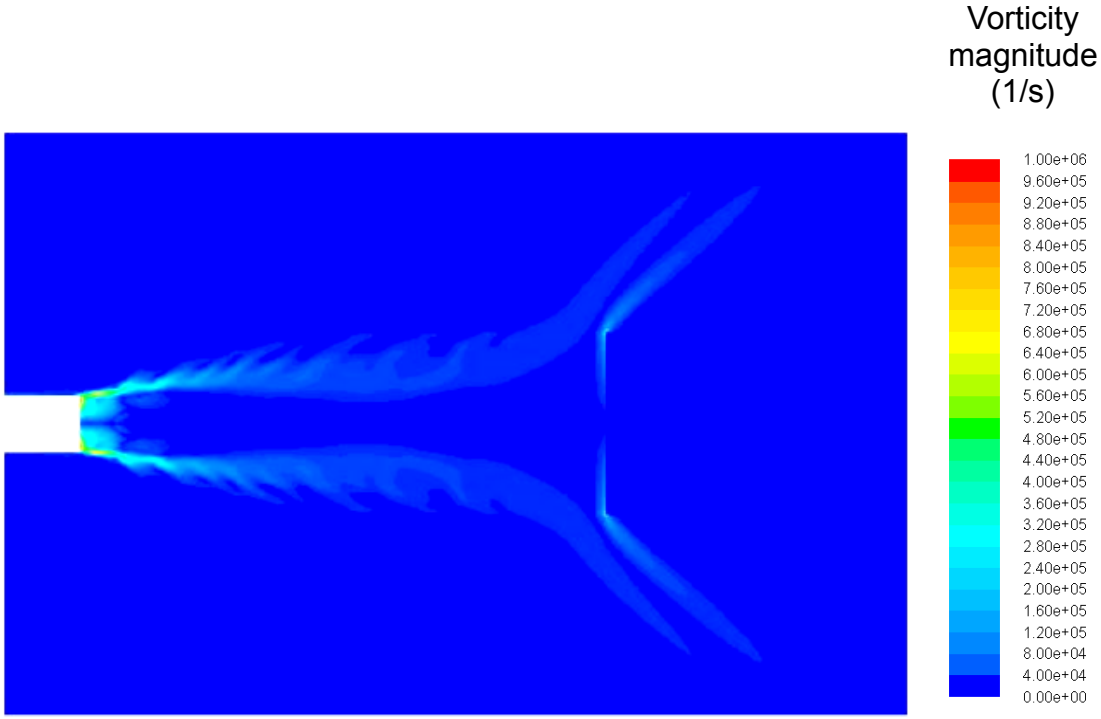

Figure 4.2 Preliminary result of the effect of substrate on the main flow, stand-off distance of 6cm, vorticity magnitude (1/s)

- Different shapes of substrate (convex and concave) at different distances from the gun should be studied; and the effect of them on flow, and deposition rate of particles on these substrates should be investigated.
- Large eddy simulation (LES) can be used instead of RSM to better simulate the turbulent flow specifically near the substrate .
- Plasma as Non Local Thermodynamic Equilibrium (NLTE) phenomenon can be modeled.

Accomplishments

Conference Papers

F. Jabbari, M. Jadidi, R. Wuthrich, and A. Dolatabadi, *A Numerical Study of Suspension Injection in Plasma-Spraying Process,* (ITSC) Conference and Exposition, May 13-15, 2013, (Busan, Republic of Korea)

M. Jadidi, F. Jabbari, M. Mousavi, A. Dolatabadi, *A Three-Dimensional Analysis of the Suspension Plasma Spray Process: The Effect of Substrate Location and Shape*, (ITSC) Conference and Exposition, 2014, Barcelona, Spain (Abstract is accepted)

Journal Paper

F. Jabbari, M. Jadidi, R. Wuthrich, and A. Dolatabadi, *A Numerical Study of Suspension Injection in Plasma-Spraying Process,* Oct 2013, J. Therm. Spray Technol., DOI (10.1007/s11666-013-0030-9).

References:

1. **Pawlowski**, **L.**, *The Science and Engineering of Thermal Spray Coatings*, 2nd edition, John Wiley & Sons, Chichester, U.K., 2008

2- **Fauchais, P.,** *Understanding Plasma Spraying*, Journal of Physics D: Applied Physics, Vol. 37, pp 86-108, 2004.

3- **Fauchais, P. and Vardelle, A.,** *Thermal Plasmas*, IEEE Transactions on Plasma Science, Vol. 25(6), pp 1258-1280, 1997.

4- **Fazilleau, J., Delbos, C., Rat, V., Coudert, J.F., Fauchais, P. and Pateyron, B.** *Phenomena Involved in Suspension Plasma Spraying Part 1: Suspension Injection and Behavior*, Plasma Chem. Plasma Process, 2006, **26**(4), p 371-391

5- **Trelles, J.P., Chazelas, C., Vardelle, A. and Heberlein**, **J.V.R.,** *Arc Plasma Torch Modeling,* J. Therm. Spray Technol., 2009, **18**(5-6), p 728-752

6- **Bolot, R., Imbert, M. and Coddet**, **C.,** *Mathematical Modeling of a Free Plasma Jet Discharging into Air and Comparison with Probe Measurements*, Thermal Spray 1997: A United Forum for Scientific and Technological Advances, C.C. Berndt Ed., 1997 (Ohio, USA), ASM International, 1997, p 549-555

7- **Bolot, R., li, J. and Coddet, C.,** *Modeling of Thermal Plasma Jet: A Comparison Between PHOENICS and FLUENT,* LERMPS-UTBM, Belfort/F.

8- **Bolot, R., li, J. and Coddet, C.,** *Some Key Advice for the Modeling of Plasma Jets Using FLUENT,* Belfort/F

9- **Ramshaw, J. D. and Chang, C. H.,** *Computational Fluid Dynamics Modeling of Multidimensional Thermal Plasma*, Plasma chemistry and plasma processing, September 1999, Volume 12, Issue 3, pp 299-325

10- **Jabbari, F., Jadidi, M., Wuthrich, R. and Dolatabadi, A.,** *A Numerical Study of Suspension Injection in Plasma-Spraying Process,* (ITSC) Conference and Exposition, May 13-15, 2013, (Busan, Republic of Korea), 2013

11- **Jabbari, F., Jadidi, M., Wuthrich, R. and Dolatabadi, A.,** *A Numerical Study of Suspension Injection in Plasma-Spraying Process,* Oct 2013, J. Therm. Spray Technol., DOI (10.1007/s11666-013-0030-9).

12- **Remesh, K., Yu, S.C.M., Ng, H.W. and Berndt**, **C.C.,** *Computational Study and Experimental Comparison of the In-Flight Particle Behavior for an External Injection Plasma Spray Process*, J. Therm. Spray Technol., 2003, 12(4), p 508-522

13- **Vincent, S., Balmigere, G., Caruyer, C., Meillot, E., Caltagirone**, **J.P.,** *Contribution to the modeling of the interaction between a plasma flow and a liquid jet*, Surf. Coating Technol., 2009, 203, p 2162-2171

14- **Meillot, E., Vincent, S., Caruyer, C., Caltagirone, J.P. and Damiani**, **D.,** *From DC Time-Dependent Thermal Plasma Generation to Suspension Plasma-Spraying Interactions*, J. Therm. Spray Technol., 2009, 18, p 875-886

15- **Caruyer, C., Vincent, S., Meillot, E., Caltagirone**, **J.P.,** *Modeling the first instant of the interaction between a liquid and a plasma jet with a compressible approach*, Surf. Coating Technol., 2010, 205, p 974-979

16- **Shan, Y., Coyle, T.W., Mostaghimi, V.,** *Numerical Simulation of Droplet Breakup and Collision in the Solution Precursor Plasma Spraying,* J. Therm. Spray Technol., 2007, 16, p 698-704

17- **Dongmo, E., Killinger, A., Wenzelburger, M., Gadow, R.,** *Numerical Approach and Optimization of the Combustion and Gas Dynamics in High Velocity Suspension Flame Spraying (HVSFS),* Surf. Coating Technol., 2009, 203, p 2139-2145

18- **Fauchais, P., Etchart-Salas, R., Rat,V., Coudert, J.F., Caron, N. and Wittmann-Teneze, K.,** *Parameters Controlling Liquid Plasma Spraying: Solutions, Sols, or Suspensions*, J. Therm. Spray Technol., 2008, 17(1), p 31-59

19- **Marchand, C., Vardelle, A., Mariaux, G., Lefort, P.,** *Modeling of the Plasma Spray Process with Liquid Feedstock Injection,* Surf. Coating Technol., 2008, 202, p 4458-4464

20- **Marchand, C., Chazelas, C., Mariaux, G., Vardelle, A.,** *Liquid Precursor Plasma Spraying: Modeling the Interactions Between the Transient Plasma Jet and the Droplets*, J. Therm. Spray Technol., 2007, 16, p 705-712

21- **Gozali, E., Kamnis, S., Gu, S.,** *Numerical Investigation of Combustion and Liquid Feedstock in High Velocity Suspension Flame Spraying Process,* Surf. Coating Technol., 2013, Article in press, doi: 10.1016/j.surfcoat.2013.04.026

22- **Aghasibeig, M., Mousavi, M., Ettouill, F.B., Wuthrich, R., Dolatabadi, A. and Moreau, C.,** *Electro-Catalytically Active Porous Nickel-Based Electrode Coatings Formed by Atmospheric and by Suspension Plasma Spraying*, International Thermal Spray (ITSC) Conference and Exposition, May 13-15, 2013, (Busan, Republic of Korea), 2013

23- **Birry, L. and Lasia, A.,** *Studies of the Hydrogen Evolution Reaction on Raney Nickel-Molybdenum Electrodes*, J. Appl. Electrochem., 2004, 34, p 735-749

24- **Boulos,** M**.I., Fauchais, P. and Pfender, E.,** *Thermal Plasmas: Fundamentals and Application*, Vol. 1, Plenum Press, New York, USA, 1994

25- ANSYS Inc., *ANSYS FLUENT Theory Guide*, USA, 2011

26- **Wan, Y.P., Sampath, S., Prasad, V., Williamson, R. and Fincke, J.R.,** *An Advanced Model for Plasma Spraying of Functionally Graded Materials.* J. Mater. Process. Technol., 2003, 137(1–3), p 110-116

27- **Boussagol, A., Mariaux, G., Legros, E., Vardelle, A. and Nylen, P.,** *3-D Modeling of a D.C. Plasma Jet Using Different Commercial CFD Codes,* Proc. 14th Int. Symp. On Plasma Chemistry, 2000, (Orleans, France), 2000

28- **Wan, Y. P., Gupta, V., Deng, Q., Sampath, S., Parsad, V., Williamson, R. and Fincke**, **J. R.,** *Modeling and Visualization of Plasma Spraying of Functionally Graded Materials and Application to the Optimization of Spray Conditions*, 2000, JTTEES 10:382-389

29- **Launder, B.E. & D.B. Spalding,** *The numerical computation of turbulent flows,* Computer Methods in Applied Mechanics and Engineering 3 *(2): 269-289, ISSN00457825*

30- **Sarkar, S. and Lakshmanan, B.,** *Application of a Reynolds Stress Turbulence Model to the Compressible Shear Layer*, AIAA Journal, Vol. 29(5), pp 743-749, 1991.

31- **Gibson, M.M. and Launder, B.E.,** *Ground Effects on Pressure Fluctuations in the Atmospheric Boundary Layer*, Journal of Fluid Mechanics, Vol. 86, pp 491-511, 1978.

32- **Launder, B.E. and Shima, N.,** *Second-Moment Closure for the Near Wall Sub-Layer: Development and Application*, AIAA Journal, Vol. 27(10), pp 1319-1325, 1989.

33- **Lien, F.S. and Leschziner, M.A.,** *Assessment of Turbulent Transport Models Including Non-Linear RNG Eddy-Viscosity Formulation and Second-Moment Closure*, Journal of Computers and Fluids, Vol. 23(8), pp 983-1004, 1994.

34- **Tanvir, S. and Qiao, L.,** *Surface Tension of Nanofluid-Type Fuels Containing Suspended Nanomaterials*, Nanoscale Res. Lett., 2012, **7**:226

35- **Ranz, W.E. and Marshall, W.R.,** *Evaporation from Drops: Part I*, Journal of Chemical Engineering Progress, Vol. 48(3), pp 141-146, 1952.

36- **Ranz, W.E. and Marshall, W.R.,** *Evaporation from Drops: Part II*, Journal of Chemical Engineering Progress, Vol. 48(4), pp 173-180, 1952.

37- **Reitz, R. D.,** *Mechanisms of Atomization Processes in High-Pressure Vaporizing Sprays*. Atomization and Spray Technology. 3. 309–337. 1987.

38- **Brossa, M. and Pfender**, **E.,** *Probe Measurements in Thermal Plasma Jets, Plasma* Chem. Plasma Process, 1988, **8**, p 75-90

Appendix

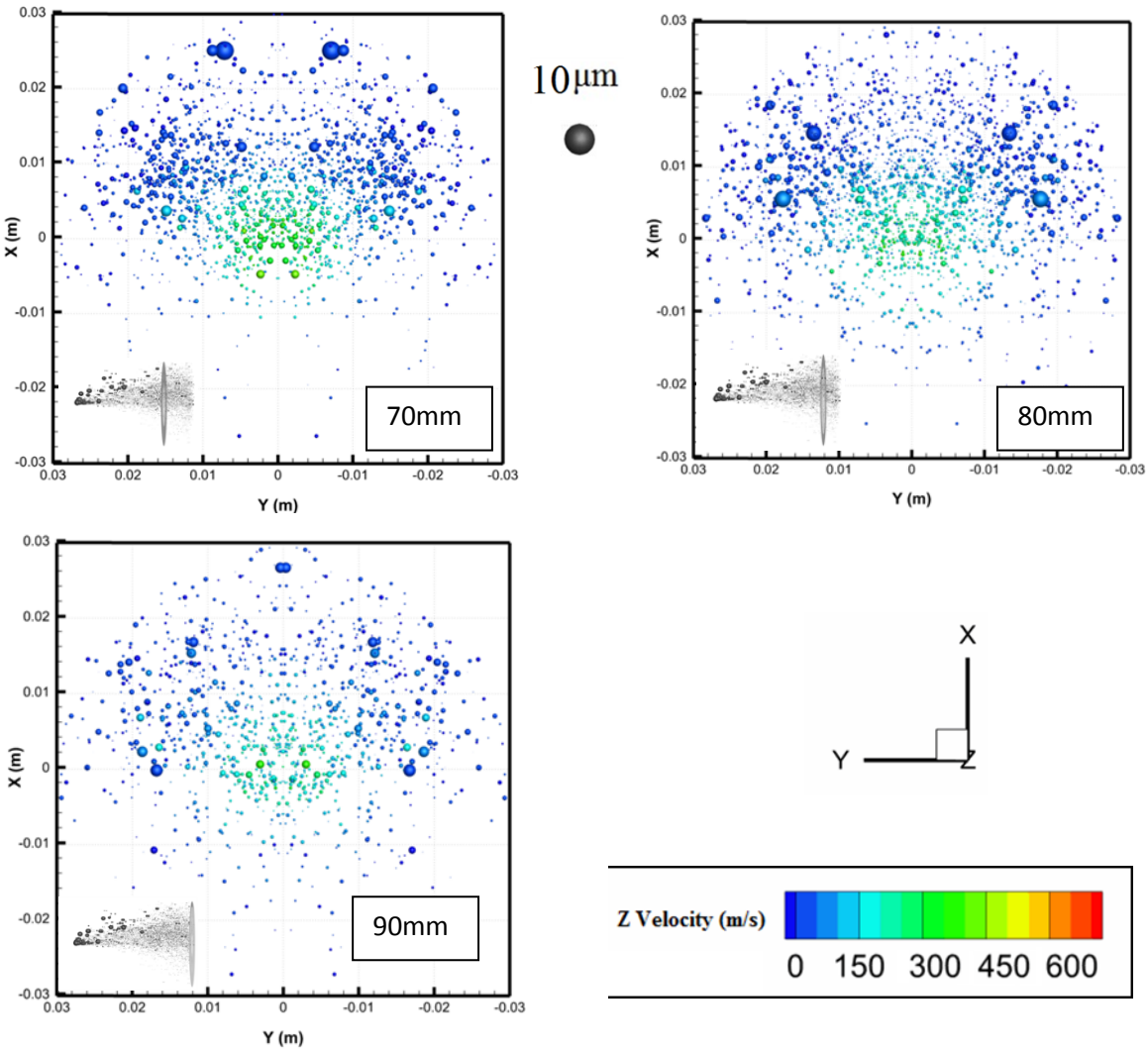

Figure 1 Case 2particle distributions in different distance from the Nozzle, Color shows Velocity of particles in Z direction and magnification is 200 times

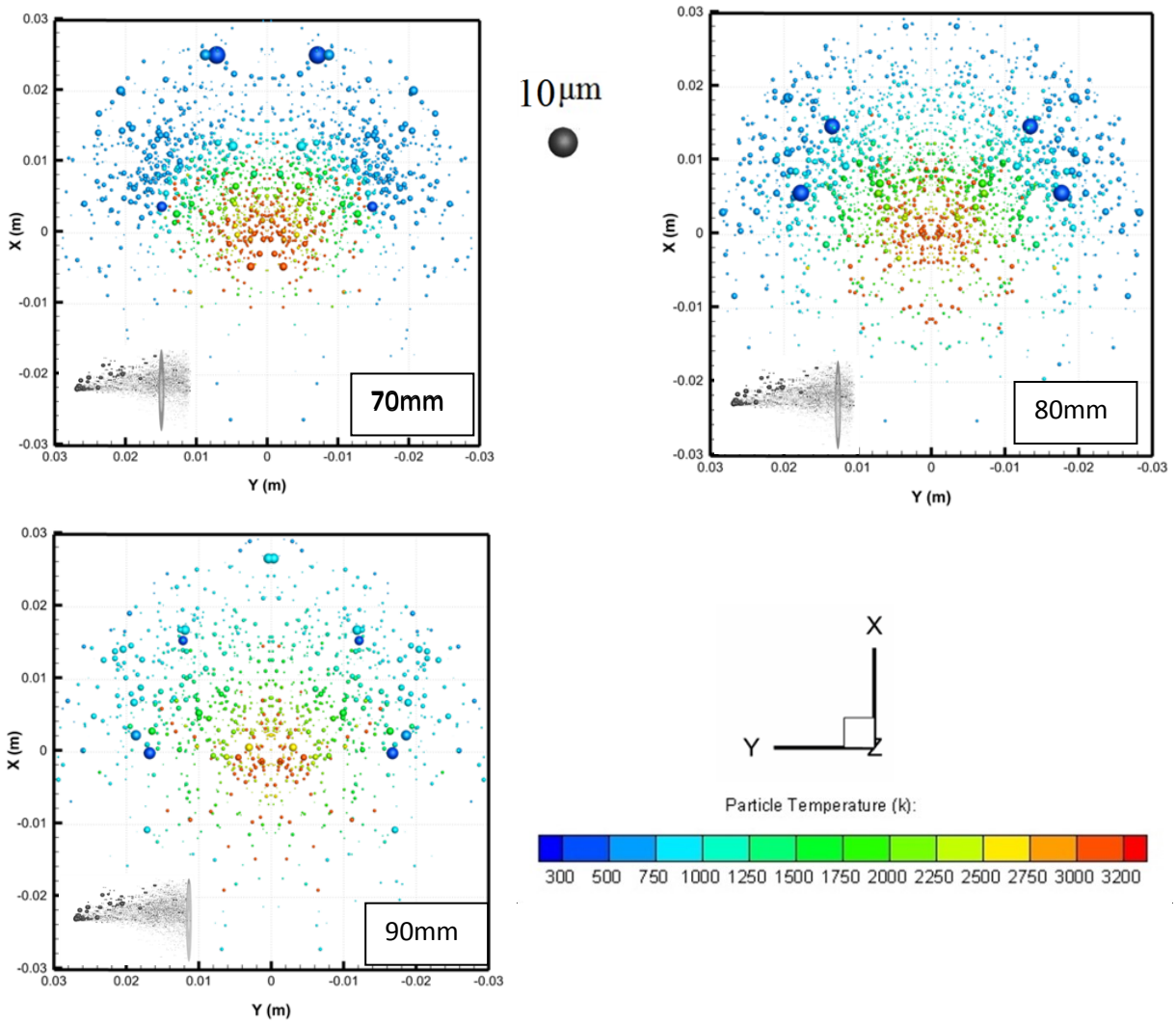

Figure 2 Case 1 particle distributions in different distance from the Nozzle, Color shows temperature of particles and magnification is 200 times

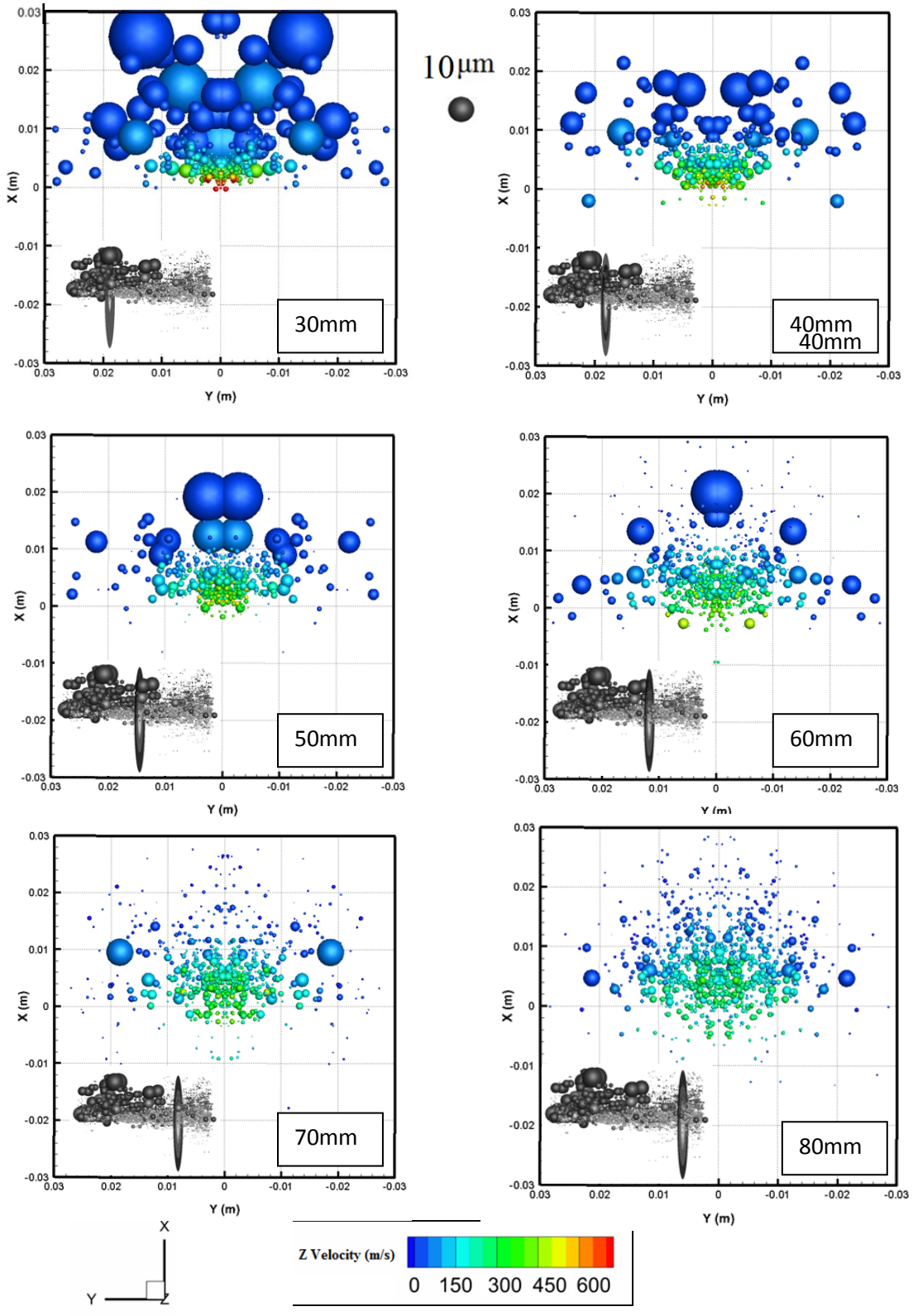

Figure 3 Case 2 particle distributions in different distance from the Nozzle, Color shows velocity of particles in Z direction and magnification is 200 times

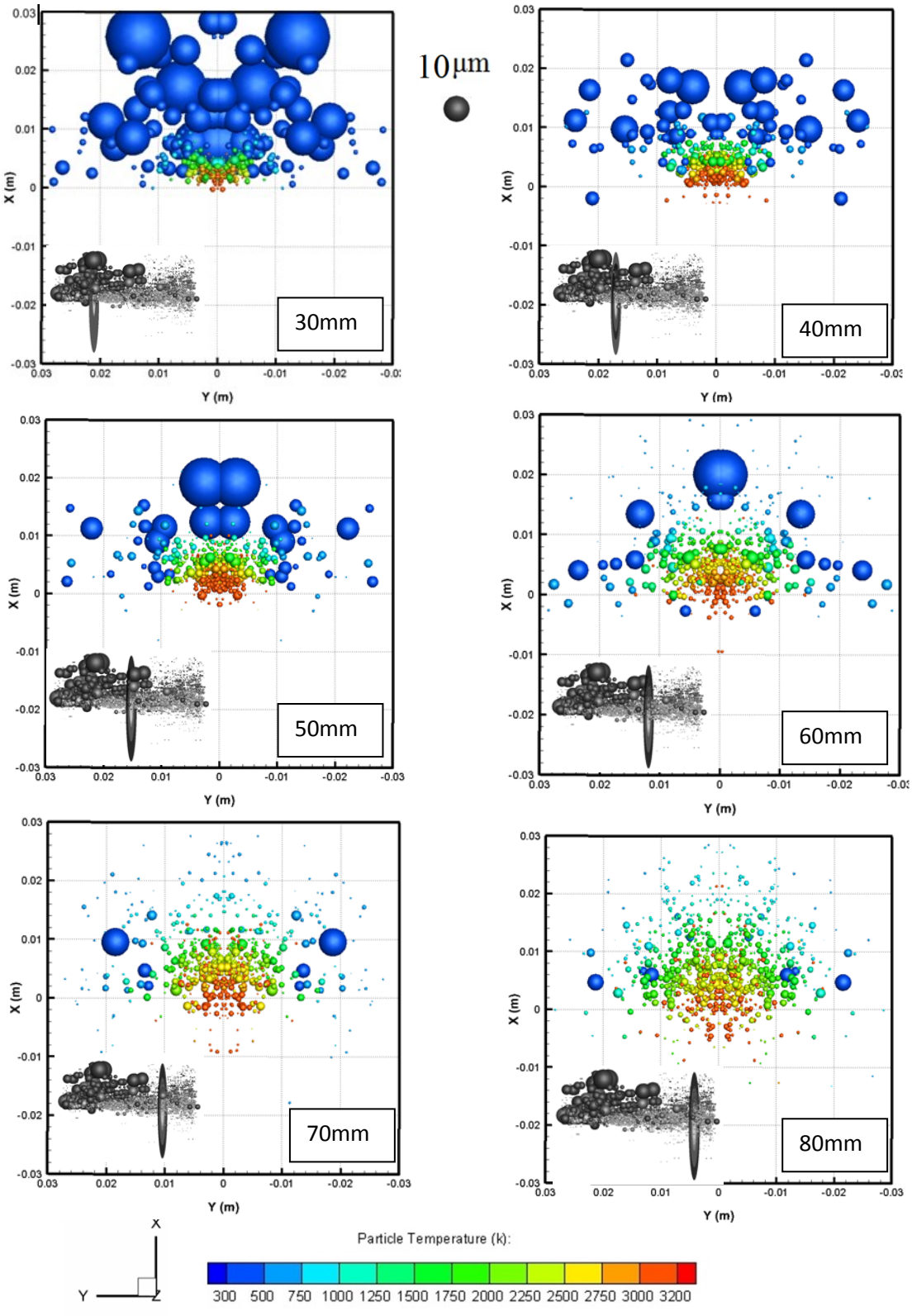

Figure 4 Case 2 particle distributions in different distance from the Nozzle, Color shows temperature of particles and magnification is 200 times

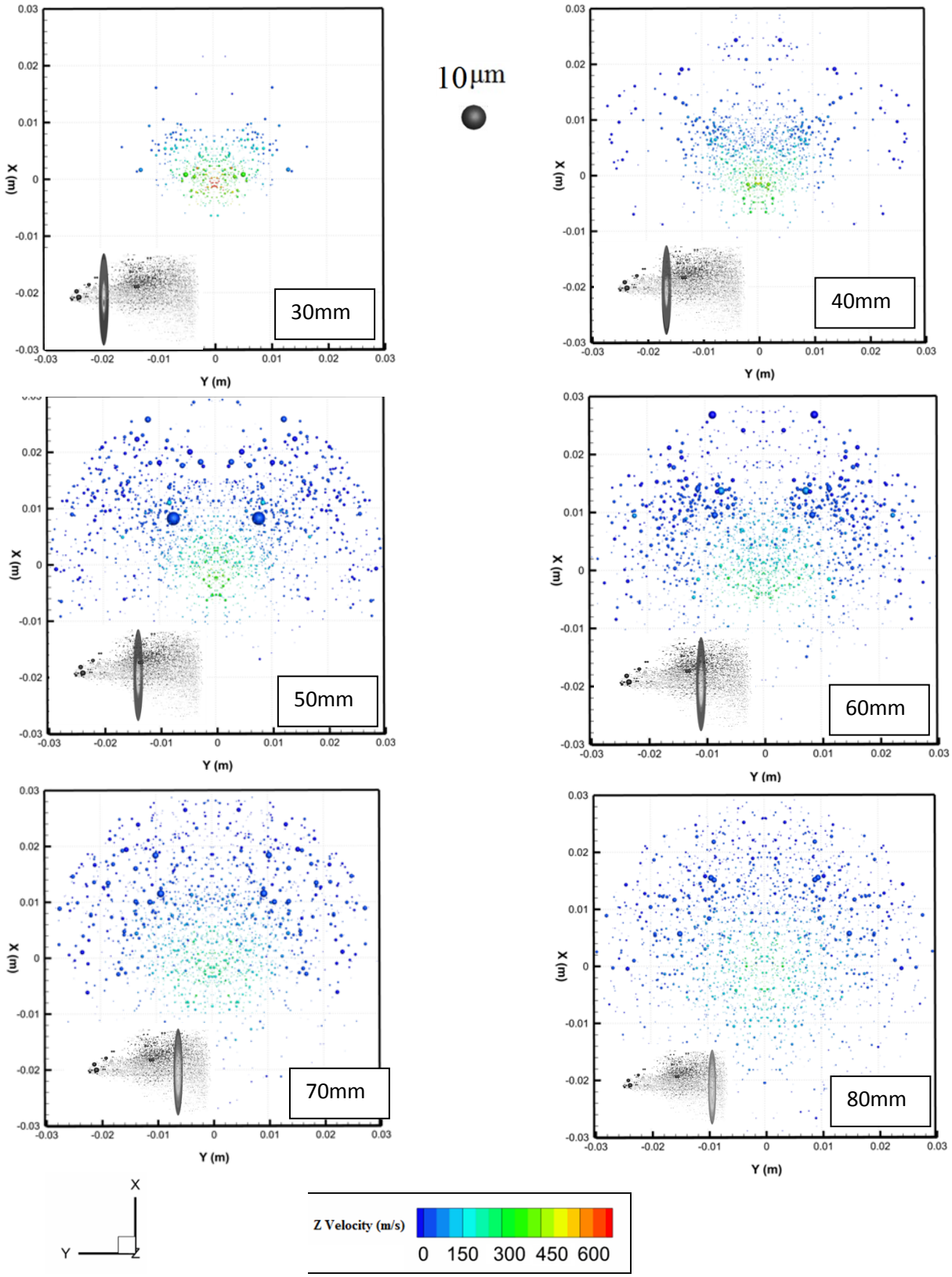

Figure 5 Case 3 particle distributions in different distance from the Nozzle, Color shows velocity of particles in Z direction and magnification is 200 times

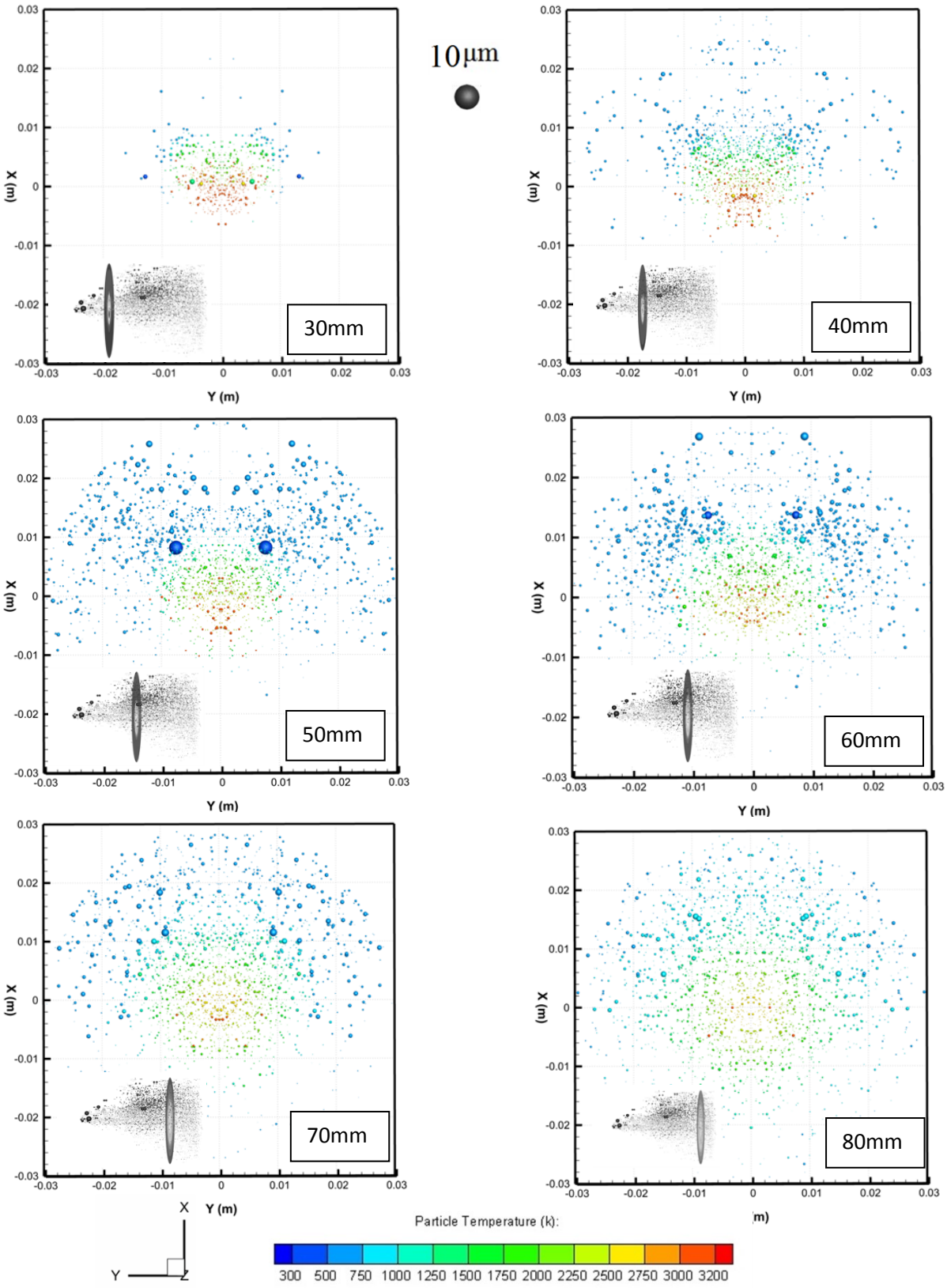

Figure 6 Case 3 particle distributions in different distance from the Nozzle, Color shows temperature of particles and magnification is 200 times